

**Three-body bremsstrahlung and the rotational character of the  $^{12}\text{C}$  spectrum**E. Garrido,<sup>1</sup> A. S. Jensen,<sup>2</sup> and D. V. Fedorov<sup>2</sup><sup>1</sup>*Instituto de Estructura de la Materia, IEM-CSIC, Serrano 123, E-28006 Madrid, Spain*<sup>2</sup>*Department of Physics and Astronomy, Aarhus University, DK-8000 Aarhus C, Denmark*

(Received 2 March 2015; published 18 May 2015)

The electric quadrupole transitions between  $0^+$ ,  $2^+$ , and  $4^+$  states in  $^{12}\text{C}$  are investigated in a  $3\alpha$  model. The three-body wave functions are obtained by means of the hyperspherical adiabatic expansion method, and the continuum is discretized by imposing a box boundary condition. Corresponding expressions for the continuum three-body ( $3\alpha$ ) bremsstrahlung and photon dissociation cross sections are derived and computed for two different  $\alpha$ - $\alpha$  potentials. The available experimental energy dependence is reproduced and a series of other cross sections are predicted. The transition strengths are defined and derived from the cross sections, and compared to schematic rotational model predictions. The computed properties of the  $^{12}\text{C}$  resonances suggest that the two lowest bands are made, respectively, by the states  $\{0_1^+, 2_1^+, 4_2^+\}$  and  $\{0_2^+, 2_2^+, 4_1^+\}$ . The transitions between the states in the first band are consistent with the rotational pattern corresponding to three alphas in an equilateral triangular structure. For the second band, the transitions are also consistent with a rotational pattern, but with the three alphas in an aligned arrangement.

DOI: [10.1103/PhysRevC.91.054003](https://doi.org/10.1103/PhysRevC.91.054003)

PACS number(s): 23.20.-g, 21.60.Gx, 21.45.-v, 27.20.+n

**I. INTRODUCTION**

The structure of the  $^{12}\text{C}$  spectrum has attracted a lot of attention along the years. In this nucleus only two bound states exist, the  $0_1^+$  ground state and the first excited state, with angular momentum and parity  $2_1^+$  and excitation energy of 4.44 MeV. We use  $J_i^\pi$  to represent the  $i$ th state with angular momentum  $J$  and parity  $\pi$ . Already in the 1950s, Hoyle predicted the existence of a  $0_2^+$  resonance at an excitation energy of 7.65 MeV, as a requirement in order to explain the known abundance of carbon in the Universe [1]. The existence of such resonance was experimentally confirmed just a few years later [2]. Its properties have recently been thoroughly reviewed [3]. Since then, many other resonant states have been observed in  $^{12}\text{C}$  [4–9]. Among them, one of the most elusive ones has been the second  $2_2^+$  state, which was predicted by different theoretical methods to have an excitation energy of around 10 MeV [10–12]. Recent experiments have confirmed the existence of this  $2_2^+$  resonance at the expected energy [5,7,8,13].

Together with the  $0^+$  and  $2^+$  states mentioned above, a  $4^+$  resonance is known to be at an excitation energy of 14.1 MeV [4,6]. Other  $4^+$  states have also been obtained numerically. In fact, the known  $4^+$  resonance is usually found to be the  $4_2^+$  state, and a first resonance at a lower energy is often obtained (for instance, at 11 MeV in Ref. [14] or 10.5 MeV in Ref. [10]). Experimental evidence of the  $4_1^+$  state was reported in Ref. [15], and its excitation energy was given to be  $13.3 \pm 0.2$  MeV, only about 1 MeV lower than the  $4_2^+$  state.

The appearance of the  $\{0^+, 2^+, 4^+\}$  sequences in the energy spectrum suggests the rotational character of these states. Therefore, at least two rotational bands could exist in  $^{12}\text{C}$ , one of them sitting on the ground state, and another one sitting on the Hoyle state. In fact, it is becoming very common in the literature to refer to these states as rotational states [16,17].

The rotational sequences of states are not necessarily  $\{0^+, 2^+, 4^+\}$  since the underlying intrinsic shapes different from axial and  $R_2(\pi)$  symmetry may provide additional states

in a given band. This is the classical knowledge that the quantum numbers specifying the states in a rotational band directly carry information about the symmetry of the intrinsic state. The details of consequences of the  $D_{3h}$  symmetry (equilateral triangle) for the  $3\alpha$  spectrum of  $^{12}\text{C}$  was formulated and discussed in general in Ref. [18]. Evidence for that symmetry was provided in Ref. [9] by comparing energy sequences and transition probabilities. We emphasize that also this model treats the resonances as bound states where all strengths are collected in the corresponding bound-state wave function.

A simple rotational sequence is also observed in  $^8\text{Be}$ , where the ground state and the two first excited states follow as well the angular momentum and parity sequence  $0^+$ ,  $2^+$ , and  $4^+$  (also  $6^+$  and  $8^+$  states with large widths, are found numerically as poles of the  $S$  matrix). All the states in the  $^8\text{Be}$  spectrum are unbound (resonances), with the ground state only about 0.1 MeV above the threshold for emission of two alpha particles. Therefore, the question arises about a possible rotational (or in general collective) character for a sequence of continuum states of considerable width. This problem was recently investigated in previous works [19–21]. This was done by computation of the electric quadrupole cross sections for bremsstrahlung emission after transitions between the  $^8\text{Be}$  states, which were described as two-body systems made of two alpha particles. These calculations required a careful treatment of the continuum wave functions and clarification of the definition of the cross section for transitions between states with a none well-defined energy.

From these  $^8\text{Be}$  cross sections it is possible to extract the transition strengths, which for the case of transitions within a rotational band must follow well-established rules based on the assumption that all the states have the same intrinsic spatial structure (rigid rotor). The main conclusion was that the computed transition strengths do not behave as expected for states in a rotational band. In fact, when increasing the angular momentum of the initial states, the transition strength was found to decrease, which is precisely the opposite to the

prediction of the rotational model [20]. Nevertheless, allowing the separation between the two alphas in the  $^8\text{Be}$  resonances to change according to the computed root mean square radius, a very nice agreement between the computed strengths and the rotational model predictions was observed.

The purpose of this work is to extend the  $^8\text{Be}$  continuum investigations to the spectrum of  $^{12}\text{C}$ , and check if the  $\{0_1^+, 2_1^+, 4_1^+\}$  and  $\{0_2^+, 2_2^+, 4_2^+\}$  sequences of states follow the behavior predicted by the rotational model. For this aim we shall compute the electric quadrupole  $\gamma$ -emission bremsstrahlung cross sections for the different transitions between the states. These cross sections and the transition strengths are not well-defined quantities when involving resonances with finite width. Suitable definitions are necessary to be specific. We shall work entirely within the strict two- and three-body framework. This means that the constituent particles are inert  $\alpha$  particles, and the interparticle nucleonic Pauli principle will be accounted for without use of the intrinsic microscopic structure. This model, used throughout this paper, can naturally be referred to as an  $\alpha$ -particle model, in contrast to microscopic  $\alpha$ -cluster models where the intrinsic nucleonic composition of the  $\alpha$  particle is the basic ingredient [12,14]. This procedure follows very closely the one described and tested in Ref. [21] for the two-body system of  $^8\text{Be}$ . In this way we can test the validity of the generalization to three-body systems.

The structure of  $^{12}\text{C}$  will be approximated as a three-alpha system and calculated by use of the hyperspherical adiabatic expansion method [22]. The continuum spectrum will be discretized by imposing a box boundary condition in the hyperradial coordinate, and the corresponding wave functions will be computed on the real energy axis, without any particular treatment of the resonances. All states are equally treated as continuum states characterized by energy, angular momentum, and parity. A resonance would only be a distribution of these discretized continuum states.

Two different alpha-alpha potentials will be used in our calculations: the Ali-Bodmer and the Buck potentials [23,24]. These potentials are parametrized to reproduce  $\alpha$ - $\alpha$  scattering properties and consequently the two-body wave functions must be the same at large distances. However, both small distances and high partial wave properties can differ drastically. All the available versions of the Ali-Bodmer potential reproduce the experimental  $s$ - and  $d$ -wave phase shifts, but only versions “d” and “e” reproduce also the ones for  $\ell = 4$  [23]. For this reason, we have chosen to use the version “d” of the Ali-Bodmer potential which has no bound states in contrast to the Buck potential [24]. Nevertheless, as shown in Ref. [20], Ali-Bodmer and Buck potentials give rise to very similar phase shifts for  $\ell = 0, 2, 4, 6$ , and 8.

The main difference between the two potentials is that the Buck potential contains two  $s$ -wave and one  $d$ -wave Pauli-forbidden bound states. This fact implies a very different short-distance behavior for the  $0^+$  and  $2^+$  wave functions in  $^8\text{Be}$  since the corresponding radial wave functions show a different number of nodes depending on the potential used. For this reason, observable quantities sensitive to the short-distance structure, like the photon emission, were expected to provide information about the underlying two-body potentials. As shown in Ref. [19], to our surprise, we found no significant

differences in the computed bremsstrahlung cross sections for  $^8\text{Be}$  between these potentials.

At the three-body level, things are very different. For instance, the ground state in  $^{12}\text{C}$  is always the lowest computed  $0^+$  state, no matter which of the two potentials is used. This is because when using the Buck potential we have two options. Either we construct the phase equivalent alpha-alpha potentials [25] or we exclude the Pauli-forbidden adiabatic potentials before computing the radial three-body wave functions [26]. In both cases the effective two-body potential shows a short-distance core repulsion, similar but not identical to the one in the Ali-Bodmer potential. As a consequence, the structure of the three-body system looks very much the same in all the cases. Therefore, we could off hand expect for  $^{12}\text{C}$  a dependence on the potential even smaller than in the  $^8\text{Be}$  case. This point will be tested in our calculations.

The paper is organized as follows. In Sec. II we describe the theoretical background needed to compute the cross sections. The particularization of the general expressions to the three-body case is given in Sec. III, which is divided into three subsections devoted to the three-body wave functions, the transition matrix element, and the transition strengths, respectively. In Sec. IV we focus on the three-alpha system, describing the details of the two-body potentials used in the calculation and discussing the corresponding computed  $^{12}\text{C}$  spectra. The electric quadrupole  $\gamma$ -emission cross sections are described in Sec. V. Finally, in Sec. VI we give the computed  $E2$ -transition strengths and compare with the predictions from the rotational model. We finish the paper with the summary and the conclusions. Some derivations and expressions not essential for the understanding of the paper, but important in order to make the paper self-contained, have been collected in three Appendixes.

## II. CROSS SECTION EXPRESSIONS

The photodissociation cross section for the breakup of a bound system  $A$  with angular momentum  $J_A$  into a three-body system with angular momentum  $J$  and three-body energy  $E$  ( $A + \gamma \rightarrow a + b + c$ ) is given by [21,27]

$$\sigma_\gamma^{(\lambda)}(E) = \frac{(2\pi)^3(\lambda+1)}{\lambda[(2\lambda+1)!!]^2} \left(\frac{E_\gamma}{\hbar c}\right)^{2\lambda-1} \frac{d\mathcal{B}^{(\lambda)}}{dE}(J_A \rightarrow J), \quad (1)$$

where  $\lambda$  is the multipolarity of the electromagnetic transition,  $E_\gamma$  is the photon energy ( $E_\gamma = E + |B_A|$ , where  $B_A$  is the binding energy of  $A$ ), and

$$\begin{aligned} \frac{d\mathcal{B}^{(\lambda)}}{dE}(J_A \rightarrow J) &= \frac{1}{2J_A+1} \sum_i |\langle \Phi_J^{(i)} | \hat{O}_\lambda | \Phi_{J_A} \rangle|^2 \delta(E - E_i), \quad (2) \end{aligned}$$

where we have assumed that the continuum spectrum describing the final three-body system has been discretized and the index  $i$  runs over the discrete continuum states. The wave function of the discrete state  $i$ , with energy  $E_i$ , is denoted by  $\Phi_J^{(i)}$ , and  $\Phi_{J_A}$  is the wave function of the bound state  $A$ . The electromagnetic operator with multipolarity  $\lambda$  is denoted by

$\hat{O}_\lambda$ , which for the case of electric transitions reads as

$$\hat{O}_{\lambda\mu} = e \sum_i Z_i r_i^\lambda Y_{\lambda\mu}(\Omega_i), \quad (3)$$

where  $i$  runs over the charged particles in the system, each of them with charge  $eZ_i$ , and  $r_i$  is the center of mass coordinate of particle  $i$ , whose direction is given by the angles  $\Omega_i$ .

As described in Appendix B, the photodissociation cross section  $\sigma_\gamma^{(\lambda)}(E)$  corresponding to the  $A + \gamma \rightarrow a + b + c$  process, and the one corresponding to the inverse reaction  $a + b + c \rightarrow A + \gamma$  [denoted now as  $\sigma^{(\lambda)}(E)$ ], are related through the expression

$$\frac{\sigma^{(\lambda)}(E)}{\sigma_\gamma^{(\lambda)}(E_\gamma)} = \nu! \frac{2(2J_A + 1)}{(2J_a + 1)(2J_b + 1)(2J_c + 1)} \frac{32\pi}{\kappa^5} \left(\frac{E_\gamma}{\hbar c}\right)^2, \quad (4)$$

where  $\nu$  is the number of identical particles in the three-body system,  $J_a$ ,  $J_b$ , and  $J_c$  are the total angular momenta of particles  $a$ ,  $b$ , and  $c$ , respectively, and  $\kappa$  is the three-body momentum, which is defined as  $\kappa = \sqrt{2mE/\hbar^2}$ . The mass  $m$  is the normalization mass used to define the Jacobi coordinates, which are the coordinates usually employed to describe the three-body system [22].

As seen in Eq. (4), the cross section  $\sigma^{(\lambda)}(E)$  corresponding to the radiative capture reaction  $a + b + c \rightarrow A + \gamma$  has dimensions of length to the fifth power, which corresponds to a surface in the six-dimensional space required to describe the incoming three-body system. This cross section depends through  $\kappa$  on the normalization mass  $m$ . This is related to the fact that when using the hyperspherical coordinates (which are constructed from the Jacobi coordinates), the radial coordinate, the hyperradius, depends also on  $m$ . Therefore, a given value of the hyperradius will correspond to different three-body geometries (different relative distances between the three particles) for different choices of  $m$ . As a consequence, the flux of incoming particles through a given hypersurface of radius  $\rho$  will depend on  $m$ , and therefore also the cross section, which is the outgoing flux of particles normalized with the incoming flux (see Appendix A). Note that the well-defined physical observable, independent of the choice made for the normalization mass, is the reaction rate (see Appendix B).

If we now replace the bound state  $A$  by a continuum state with energy  $E'$  and momentum  $J'$ , the photodissociation cross section for the process  $A + \gamma \rightarrow a + b + c$  given in Eq. (1) can be easily generalized as described in Ref. [21]:

$$\frac{d\sigma_\gamma^{(\lambda)}(E)}{dE'} = \frac{(2\pi)^3(\lambda + 1)}{\lambda[(2\lambda + 1)!!]^2} \left(\frac{E_\gamma}{\hbar c}\right)^{2\lambda-1} \frac{d\mathcal{B}^{(\lambda)}}{dE dE'}(J' \rightarrow J), \quad (5)$$

where  $E_\gamma = E - E'$  is the photon energy and

$$\begin{aligned} \frac{d\mathcal{B}^{(\lambda)}}{dE dE'}(J' \rightarrow J) &= \frac{1}{2J' + 1} \sum_{i,j} |(\Phi_J^{(i)} | \hat{O}_\lambda | \Phi_{J'}^{(j)})|^2 \\ &\times \delta(E - E_i) \delta(E' - E'_j), \end{aligned} \quad (6)$$

where the initial continuum states have also been discretized, and the index  $j$  runs over the initial continuum discrete states

with energy  $E'_j$  and wave function  $\Phi_{J'}^{(j)}$ . It is important to note that the summation over  $i$  and  $j$  in the equation above is not unrestricted, but limited to the initial and final energy ranges of experimental interest. We will come back to this point later on.

Finally, according to Eq. (4), we have that the cross section for the continuum-to-continuum reaction  $a + b + c \rightarrow A + \gamma$ , with initial and final energies  $E$  and  $E'$ , and initial and final angular momenta  $J$  and  $J'$  is given by

$$\begin{aligned} \frac{d\sigma^{(\lambda)}}{dE'}(E) &= \nu! \frac{2(2J_A + 1)}{(2J_a + 1)(2J_b + 1)(2J_c + 1)} \\ &\times \frac{32\pi}{\kappa^5} \left(\frac{E_\gamma}{\hbar c}\right)^2 \frac{d\sigma_\gamma^{(\lambda)}}{dE'}(E_\gamma). \end{aligned} \quad (7)$$

As discussed in Ref. [21], the total bremsstrahlung cross section, as a function of the incident energy  $E$ , is obtained after integration over  $E'$  (or over the photon energy  $E_\gamma$ ). In our description using discrete initial and final continuum states, the integral over  $E'$  is trivially made thanks to the  $\delta(E' - E'_j)$  function in Eq. (6), and just a summation over the index  $j$  running over the final discrete states remains:

$$\begin{aligned} \sigma^{(\lambda)}(E) &= \frac{\nu!}{(2J_a + 1)(2J_b + 1)(2J_c + 1)} \left(\frac{E_\gamma}{\hbar c}\right)^{2\lambda+1} \\ &\times \frac{16}{\pi} \frac{1}{\kappa^5} \frac{(2\pi)^5(\lambda + 1)}{\lambda[(2\lambda + 1)!!]^2} \\ &\times \sum_{i,j} |(\Phi_J^{(i)} | \hat{O}_\lambda | \Phi_{J'}^{(j)})|^2 \delta(E - E_i). \end{aligned} \quad (8)$$

As anticipated below Eq. (6) and stated in Ref. [19], the computed cross sections should be obtained in close analogy to the experimental setup, where only a finite range of final relative energies is measured, usually around a resonance in the final system. This means that the integral over  $E'$  has to be performed only over this precise energy range. In our language of discrete continuum states, this means that the summation over  $j$  in the equation above runs only over the final discrete states whose energy  $E'_j$  is contained in the chosen final energy window. It is obvious then that the total bremsstrahlung cross section depends on such final energy window (see [20,21]). In other words, definitive statements about resonance properties must take into account that these continuum states have an energy at best defined with an accuracy of less than its width.

### III. THREE-BODY INGREDIENTS

In order to compute the cross section given in Eq. (8) we first need the wave functions for the three interacting particles in states with given energy and specified angular momentum and parity. Then we need the transition probability from one state to another. This requires specific matrix elements which by combination of various kinematic factors provide cross sections and through proper definitions also the related transition strengths.

### A. Three-body wave functions

In this work we shall construct the three-body wave functions using the hyperspherical adiabatic expansion method described in Ref. [22]. In this method the wave function is expanded in terms of a complete set of angular functions  $\{\phi_n^J\}$ , where  $J$  is the total angular momentum of the three-body system:

$$\Phi_J = \frac{1}{\rho^{5/2}} \sum_n f_n^J(\rho) \phi_n^J(\rho, \Omega) \quad (\Omega \equiv \{\alpha, \Omega_x, \Omega_y\}), \quad (9)$$

where  $\rho = \sqrt{x^2 + y^2}$ ,  $\alpha = \arctan(x/y)$ , and  $\{\Omega_x, \Omega_y\}$  are the angles defining the directions of  $\mathbf{x}$  and  $\mathbf{y}$ , which are the Jacobi coordinates used to describe the system. Writing the Schrödinger equation in terms of these coordinates, they can be separated into angular and radial parts:

$$\hat{\Lambda}^2 \phi_n^J + \frac{2m\rho^2}{\hbar^2} (V_{jk} + V_{ik} + V_{ij}) \phi_n^J = \lambda_n(\rho) \phi_n^J \quad (10)$$

and

$$\left[ -\frac{d^2}{d\rho^2} + \frac{2m}{\hbar^2} [V_{3b}(\rho) - E] + \frac{1}{\rho^2} \left( \lambda_n(\rho) + \frac{15}{4} \right) \right] f_n^J(\rho) + \sum_{n'} \left( -2P_{nn'} \frac{d}{d\rho} - Q_{nn'} \right) f_{n'}(\rho) = 0, \quad (11)$$

where  $V_{jk}$ ,  $V_{ik}$ , and  $V_{ij}$  are the two-body interactions between each pair of particles,  $\hat{\Lambda}^2$  is the hyperangular operator (see Ref. [22]), and  $m$  is the normalization mass. In Eq. (11),  $E$  is the three-body energy, and the coupling functions  $P_{nn'}$  and  $Q_{nn'}$  are given for instance in Ref. [22]. The potential  $V_{3b}(\rho)$  is used for fine tuning to take into account all those effects that go beyond the two-body interactions.

It is important to note that the angular functions used in the expansion in Eq. (9) are precisely the eigenfunctions of the angular part of the Schrödinger (or Faddeev) equation(s). Each of them is in practice obtained by expansion in terms of the hyperspherical harmonics [see Eq. (C2)]. Obviously, this infinite expansion has to be truncated at some point, maintaining only the contributing components.

The eigenvalues  $\lambda_n(\rho)$  in Eq. (10) enter in the radial equations (11) as a basic ingredient in the effective radial potentials. Accurate calculation of the  $\lambda$  eigenvalues requires, for each particular component, a sufficiently large number of hyperspherical harmonics. In other words, the maximum value of the hypermomentum  $K_{\max}$  for each component must be large enough to assure convergence of the  $\lambda$  functions in the region of  $\rho$  values where the  $f_n^J(\rho)$  wave functions are relevant for the calculation of the electromagnetic operator matrix element.

Finally, the last convergence to take into account is the one corresponding to the expansion in Eq. (9). Typically, for bound states, this expansion converges rather fast, and usually three or four adiabatic terms are already sufficient.

In our calculations the continuum is discretized by use of a box boundary condition. This means that the radial wave functions  $f_n(\rho)$  are imposed to be zero at a given maximum value of  $\rho$ , which is typically taken equal to a few hundreds of fm ( $\rho_{\max} = 200$  fm in our calculations). No distinction is made between resonances and ordinary continuum states.

Therefore, in order to place the initial and final energy windows matching the resonance energies, it will be necessary to have some previous information about what these energies are. It also implies that the computed result simultaneously includes on-resonance as well as continuum background contributions.

### B. Transition matrix element

Once the initial and final three-body wave functions are computed, we can now obtain the square of the transition matrix element

$$|\langle \Phi_J^{(i)} | \hat{\mathcal{O}}_\lambda | \Phi_{J'}^{(j)} \rangle|^2 = (2J+1) \sum_{\mu M'} |\langle \Phi_{JM}^{(i)} | \hat{\mathcal{O}}_{\lambda\mu} | \Phi_{J'M'}^{(j)} \rangle|^2 \quad (12)$$

which enters in Eq. (8), and where  $\hat{\mathcal{O}}_{\lambda\mu}$  is the electric multipole operator given in Eq. (3).

From the definition of the Jacobi coordinates (Ref. [22]), it is not difficult to see that the vector  $\mathbf{r}_p$  giving the position of particle  $p$  can be written as

$$\mathbf{r}_p = \sqrt{\frac{m(m_q + m_s)}{m_p(m_p + m_q + m_s)}} \mathbf{y}_p, \quad (13)$$

where  $m_p$ ,  $m_q$ , and  $m_s$  are the masses of the three particles and  $\mathbf{y}_p$  is the Jacobi coordinate defined between particle  $p$  and the center of mass of the other two. Therefore, using Eq. (3), we get

$$\langle \Phi_J^{(i)} | \hat{\mathcal{O}}_\lambda | \Phi_{J'}^{(j)} \rangle = e \sum_{p=1}^3 Z_p \left( \frac{m(m_q + m_s)}{m_p(m_p + m_q + m_s)} \right)^{\lambda/2} \times \langle \Phi_J^{(i)} | |y_p^\lambda Y_\lambda(\hat{r}_p)| | \Phi_{J'}^{(j)} \rangle, \quad (14)$$

and the calculation of the reduced matrix element in Eq. (12) requires only the calculation of the matrix element  $\langle \Phi_J^{(i)} | |y_p^\lambda Y_\lambda(\hat{r}_p)| | \Phi_{J'}^{(j)} \rangle$  for each of the three possible definitions of the Jacobi coordinate  $\mathbf{y}_p$ . This reduced matrix element is obtained as described in Appendix C. The final expression in Eq. (C4) is rather elaborate although mostly due to the Racah algebra necessary to account correctly for all total angular momentum couplings in general cases of particles with finite intrinsic spin.

The integral over  $\rho$  in Eq. (C4) involves the radial wave functions  $f_n^J$  and  $f_{n'}^{J'}$  corresponding to the initial and final continuum states. Therefore, the function to be integrated does not fall to zero at infinity, but instead gives rise to an apparent divergence of the necessary integrals. This divergence is obviously nonphysical and mathematically ill defined until a suitable limiting procedure is chosen. A simple way to solve this numerical problem was proposed in Ref. [21], where the integrand was multiplied by the factor  $e^{-\eta^2 \rho^2}$ , in such a way that the correct result is obtained in the limit of  $\eta = 0$ . In practice, a value of  $\eta$  in the vicinity of  $\eta = 0.01$  fm<sup>-1</sup> is enough to get a sufficient accuracy.

It is important to note that the divergence mentioned in the previous paragraph appears due to the application of the long-wavelength approximation, thanks to which the electric field can be obtained from the charge density only (Siebert theorem). This theorem leads to the electric transition multipole operator given in Eq. (3). In Ref. [28] an extension



of the Siegert theorem not relying on the long-wavelength approximation was proposed, in such a way that the divergence problem in the matrix element disappears. The equivalence between this procedure and different techniques designed to treat the divergence problem (the one used in this work among them) has been investigated in Ref. [29].

### C. Transition strength

In principle, calculation of the  $\mathcal{B}^{(E\lambda)}$  strength for the continuum-to-continuum transition  $a + b + c \rightarrow A + \gamma$  could be made directly through Eq. (6), which thanks to the  $\delta$  functions would permit to obtain the total transition strength just by summation over  $i$  and  $j$  of the square of the reduced matrix element. This would in fact be the same procedure as when a bound state is involved in the transition. However, as discussed in Ref. [20], an indiscriminate sum over initial and final continuum states makes the result rather meaningless. The information about resonance properties is completely washed out and, even worse, weighted at the wrong energies. Furthermore, due to the undesired divergence produced by the soft-photon contribution, which appears when the energy of the emitted photon approaches zero ( $E' \rightarrow E$  or  $E'_j \rightarrow E_i$ ) [19], the calculation itself is pretty complicated. For these reasons, we shall obtain the transition strength as described in Ref. [20], i.e., directly from the cross section in Eqs. (7) and (5). Two different methods will be used.

In the first method, the strength is obtained from the total (integrated) cross section. More precisely, for a transition between some initial and final energy windows, typically around some resonances in the initial and final states, integration of Eq. (7) over  $E$  and  $E'$  within those two windows will provide the total cross section for the transition. If the photon energy  $E_\gamma$  were constant, this would immediately provide the total transition strength just after division by the constants multiplying the transition strength. However, since this is not correct, we must use an average value for  $E_\gamma^{2\lambda+1}$ . In particular, the photon energy will be taken as  $E_\gamma = E_c - E'_c$  where  $E_c$  is the energy of the cross section peak corresponding to the resonance in the initial state and  $E'_c$  is the center of the final energy window (usually the resonance energy in the final state). Of course, this procedure assumes information about resonance positions, and it can be sensitive to rather small variations around a chosen  $E_\gamma$  owing to the power of  $(2\lambda + 1)$  for  $\mathcal{B}(E\lambda)$  transitions (see Ref. [19] for details).

The second method exploits the fact that in the vicinity of a resonance the cross section of the photo-dissociation reaction  $A + \gamma \rightarrow a + b + c$  takes the form

$$\sigma_\gamma(E_\gamma) = \frac{2J + 1}{2(2J_A + 1)} \frac{\pi \hbar^2 c^2}{E_\gamma^2} \frac{\Gamma_R \Gamma_\gamma}{(E - E_R)^2 + \Gamma^2/4}, \quad (15)$$

where after the collision the particles  $a$ ,  $b$ , and  $c$  are assumed to populate a resonance with angular momentum  $J$ , energy  $E_R$ , and width for decay into three particles  $\Gamma_R$ .  $J_A$  is the angular momentum of  $A$  and  $\Gamma = \Gamma_R + \Gamma_\gamma$ , where  $\Gamma_\gamma$  is the  $\gamma$ -decay width of the three-body resonance.

Using Eq. (4), we can easily obtain the expression equivalent to Eq. (15) for the inverse cross section after the three-body

collision  $a + b + c \rightarrow A + \gamma$ , which can be written as

$$\sigma(E) = \frac{v!(2J + 1)}{(2J_a + 1)(2J_b + 1)(2J_c + 1)} \frac{8(2\pi)^2}{\kappa^5} \times \frac{\Gamma_R \Gamma_\gamma}{(E - E_R)^2 + \Gamma^2/4}, \quad (16)$$

where now the three colliding particles, with spins  $J_a$ ,  $J_b$ , and  $J_c$  are assumed to populate a three-body resonance with angular momentum  $J$ , energy  $E_R$ , and width for decay into three particles  $\Gamma_R$ .

The second method uses the value of  $\Gamma_\gamma$  in the equation above in order to fit the peak in the computed cross section in Eq. (8) corresponding to the three-body resonance at  $E = E_R$ , in such a way that from  $\Gamma_\gamma$  we can obtain the transition strength thanks to the well-known expression [30]

$$\Gamma_\gamma = \frac{8\pi(\lambda + 1)}{\lambda[(2\lambda + 1)!!]^2} \left(\frac{E_\gamma}{\hbar c}\right)^{2\lambda+1} \mathcal{B}^{(E\lambda)}(J \rightarrow J_A). \quad (17)$$

The two methods can be compared. The first prescription depends on the windows chosen for both initial and final states. These choices should be made precisely to reproduce the conditions in a given measurement. However, then the average photon energy becomes important. The second prescription relies on the behavior of the cross section for energies around the resonance peak. This dependence is assumed to have the Breit-Wigner shape with the advantage (and related weakness) that only a few points around the peak are used. The photon energy does not enter as a multiplicative factor, but deviations from the assumed simple Lorentzian behavior are not accounted for.

## IV. THREE-ALPHA SYSTEM

In this section we describe the calculation made to construct the wave functions for a system of three alpha particles. We start giving the details of the two-body  $\alpha$ - $\alpha$  potentials used in the calculation and some properties of the  $^8\text{Be}$  spectrum. In the second part we summarize the properties of the  $^{12}\text{C}$  spectrum.

### A. $^8\text{Be}$ properties

We shall consider the same two  $\alpha$ - $\alpha$  potentials used in Ref. [20], i.e., the Buck potential [24] and version  $d$  of the Ali-Bodmer potential given in Ref. [23]. The Buck potential has two spurious deep-lying  $\alpha$ - $\alpha$  bound states for  $s$  waves and one more for  $d$  waves. These spurious states correspond to Pauli-forbidden states. On the contrary, the Ali-Bodmer potential is a shallow potential not holding any bound  $\alpha$ - $\alpha$  state. These two potentials give rise to very similar  $\ell = 0, 2, 4, 6$ , and  $8$  phase shifts.

The spectrum of  $^8\text{Be}$  obtained with these two potentials is discussed in Ref. [20]. In here we only summarize in Table I the energies and widths of the different states. The first two rows show the known experimental energies and widths [31] of the  $0^+$ ,  $2^+$ , and  $4^+$  resonances in  $^8\text{Be}$ . The experimental values are well reproduced by both potentials. The computed resonances have been obtained as poles of the  $\mathcal{S}$  matrix by use of the complex scaling method [32,33]. The widths of the

TABLE I. Properties of the five lowest computed resonances in  ${}^8\text{Be}$ . The first two rows give, when available, the corresponding experimental energies  $E_r$  and widths  $\Gamma_r$  taken from Ref. [31]. The computed values with the Buck and Ali-Bodmer potentials are given by the third and fourth rows, and by the fifth and sixth rows, respectively. All the energies and widths are given in MeV. The following four rows give, also for the two  $\alpha$ - $\alpha$  potentials, the real and imaginary parts of  $\sqrt{\langle r^2 \rangle}$ , computed with the complex scaling method. These values are given in fm.

$J^+$	$0^+$	$2^+$	$4^+$	$6^+$	$8^+$
$E_r$ (Expt.)	0.0918	$2.94 \pm 0.01$	$11.35 \pm 0.15$		
$\Gamma_r$ (Expt.)	$(5.57 \pm 0.25)10^{-6}$	$1.51 \pm 0.02$	$\sim 3.5$		
$E_r$ (Buck)	0.091	2.88	11.78	33.55	51.56
$\Gamma_r$ (Buck)	$3.6 \times 10^{-5}$	1.24	3.57	37.38	92.38
$E_r$ (Ali-Bodmer d)	0.092	2.90	11.70	34.38	53.65
$\Gamma_r$ (Ali-Bodmer d)	$3.1 \times 10^{-6}$	1.27	3.07	37.19	93.74
$\text{Re}\sqrt{\langle r^2 \rangle}$ (Buck)	5.61	3.51	2.93	2.82	2.76
$\text{Im}\sqrt{\langle r^2 \rangle}$ (Buck)	0.01	1.29	0.82	1.44	1.77
$\text{Re}\sqrt{\langle r^2 \rangle}$ (Ali-Bodmer d)	5.80	3.58	2.91	2.70	2.73
$\text{Im}\sqrt{\langle r^2 \rangle}$ (Ali-Bodmer d)	0.001	1.24	0.76	1.40	1.73

computed  $6^+$  and  $8^+$  resonances are very big, comparable to their energies, and actually, they should not be considered as well-defined resonances.

After a complex scaling calculation, the complex rotated wave functions of the resonances fall off asymptotically as ordinary bound states. It is therefore possible to compute mean-square-radii, expectation values of  $r^2$ , which for resonances are complex numbers, in contrast to the real values obtained for bound states even if the corresponding wave functions have been complex rotated. The real and imaginary parts of  $\langle r^2 \rangle^{1/2}$  for each of the computed resonances are also given in Table I. As introduced by Berggren [34,35], and also discussed in Ref. [33], the real part of the expectation value of a given complex rotated operator has been attempted interpreted as a corresponding average value over continuum wave functions in a range of energies around the resonance. It is then tempting to associate the imaginary part of  $\langle r^2 \rangle^{1/2}$  with an uncertainty of the resonance size arising from the nonzero width of the state.

### B. ${}^{12}\text{C}$ spectrum

The resonances of the three-alpha system are obtained as described in Ref. [10]. The method follows the hyperspherical adiabatic expansion method [22] sketched in Sec. III A, which is used in combination with the complex scaling method [32,33]. The three-body resonances appear then as ordinary bound states with complex energy, whose real and imaginary parts give the resonance energy and half the width of the resonance. This method does not make any assumption about the resonance properties. For instance, the resonance decay mechanism is dictated by the dynamic evolution of the resonances, i.e., by the change in structure from small to large distances. In this way, the sequential and direct decay channels are both simultaneously taken into account, and the corresponding branching ratios are directly dictated by the resonance wave function [36].

In order to reproduce the known experimental energies in the  ${}^{12}\text{C}$  spectrum a fine tuning with a short-range three-body force is required. This is done by the potential  $V_{3b}(\rho)$

introduced in the set of radial equations given in Eq. (11). As in Ref. [10], we shall consider here a Gaussian three-body potential  $V_{3b} = S e^{-\rho^2/b^2}$ , where the range  $b$  is taken equal to 6 fm, which approximately corresponds to the hyperradius obtained from three touching  $\alpha$  particles. This  $V_{3b}$  construction maintains the structure of a three-body state, but varying the strength  $S$ , the energy position can be adjusted to reproduce the measured value of the resonance.

When using the Buck potential, due to the existence of Pauli-forbidden two-body states, a direct three-body calculation gives rise to a large amount of spurious bound three-body states. To avoid this problem, the three-body calculation is made using the phase-equivalent version of the Buck potential. This potential is constructed numerically from the original one, and it provides a two-body potential with exactly the same phase shifts for all energies, but where the undesired forbidden bound states have been removed from the two-body spectrum (see Ref. [25] for details).

In Table II we give the computed energies and widths obtained for the  $0^+$ ,  $2^+$ , and  $4^+$  states, which are the states of interest for this work. The experimental data are taken from Refs. [4,7,8,15,37]. The results obtained with the Ali-Bodmer and the Buck potentials are given. For each calculation the value of the strength  $S$  used in the three-body force is also given.

For the  $0^+$  states, if the three-body force is used to fit the energy of the ground state, we then get a second  $0^+$  state (the Hoyle state) slightly bound, which is clearly incorrect. In order to get the correct energy for the Hoyle state, whose structure is expected to agree more with the three-alpha model than the ground state, it is therefore necessary to weaken the three-body attraction, which makes the ground state underbound by a bit more than 1 MeV. When this is done, a third  $0^+$  state appears at an energy of about 5.5 MeV with the Ali-Bodmer potential and 4 MeV with the Buck potential. This last energy agrees with the experimental value, although the large experimental width is better reproduced with the Ali-Bodmer potential. It is important to keep in mind that the resonances are computed as poles of the  $\mathcal{S}$  matrix, and the experimental data are often obtained after an  $\mathcal{R}$  matrix analysis of the cross sections. These

TABLE II. Calculated and measured energies  $E_R$  (in MeV) and partial  $\alpha$ -decay widths  $\Gamma_R$  (in keV) of the  $^{12}\text{C}$  resonances for different  $J^\pi$ . Experimental values (labeled “expt.”) are from [4,7,8,15,37]. The labels “AB” and “Buck” refer to the calculations obtained using the Ali-Bodmer and Buck  $\alpha$ - $\alpha$  potentials specified in Sec. IV A. The strength  $S$  (in MeV) used in the Gaussian three-body potential  $V_{3b}$  is also given for each of the calculations (the strength of the three-body force is always taken to be  $b = 6.0$  fm). The energies are measured from the three-alpha threshold.

$J^\pi$	$E_{R,\text{expt.}}$	$\Gamma_{R,\text{expt.}}$	$E_{R,\text{AB}}$	$\Gamma_{R,\text{AB}}$	$S$	$E_{R,\text{Buck}}$	$\Gamma_{R,\text{Buck}}$	$S$
$0_1^+$	$-7.275^a$		$-7.27$		$-22.6$	$-7.27$		$-22.0$
$0_2^+$	$0.380^a$	$0.009 \pm 0.001^a$	$0.38$	$\lesssim 0.05$	$-18.2$	$0.38$	$\lesssim 0.05$	$-18.0$
$0_3^+$	$4.20 \pm 0.14^b$	$3440 \pm 220^b$	$5.52$	$2200$	$-18.2$	$4.12$	$700$	$-18.0$
$2_1^+$	$-2.8356 \pm 0.0003^a$	$0.0$	$-2.84$		$-12.6$	$-2.85$		$-12.1$
$2_2^+$	$2.76 \pm 0.11^c$	$800 \pm 130^c$	$1.75/2.36$	$375/1150$	$-12.6/-3.0$	$1.72/2.35$	$161/920$	$-12.1/-3.0$
	$2.86 \pm 0.05^d$	$2080 \pm 300^d$						
$2_3^+$	$3.88 \pm 0.05^a$	$430 \pm 80^a$	$3.90/6.87$	$163/2010$	$-12.6/-3.0$	$5.04/5.48$	$570/3600$	$-12.1/-3.0$
$4_1^+$	$6.0 \pm 0.2^e$	$1700 \pm 200^e$	$5.33$	$3700$	$16.3$	$5.48$	$3800$	$13.4$
$4_2^+$	$6.81 \pm 0.02^a$	$258 \pm 15^a$	$6.82$	$620$	$16.3$	$6.81$	$800$	$13.4$
$4_3^+$			$13.1$	$1800$	$16.3$	$13.1$	$2060$	$13.4$

<sup>a</sup>Reference [4].

<sup>b</sup>Reference [37].

<sup>c</sup>Reference [7].

<sup>d</sup>Reference [8].

<sup>e</sup>Reference [15].

two different procedures can lead to sometimes very different values for the resonance widths [38]. In Table II, the two values of the strength of the three-body force  $S$  fitting the experimental energies of the  $0_1^+$  and  $0_2^+$  states, are given.

For the  $2^+$  states we proceed in a similar way. When the three-body force is used to fit the energy of the bound  $2^+$  state, we then get the second  $2^+$  state with an energy and width of (1.75, 0.38) MeV and (1.72, 0.16) MeV with the Ali-Bodmer and Buck potentials, respectively. These values of energy and width are lower than the experimental values recently given in Refs. [7,8]. Again, in order to fit this energy we have to weaken the three-body force, in such a way that the  $2_2^+$  resonance appears at about 2.4 MeV. An even weaker three-body force would place the  $2_2^+$  state at 2.8 MeV, in better agreement with the experimental value, but in this case the resonance would be too wide and more difficult to obtain through a complex scaling calculation (due to the large rotation angle required in this case). When the energy of the  $2_2^+$  resonance is placed at about 2.4 MeV, the corresponding width is around 1 MeV with both, the Ali-Bodmer and the Buck potential. This width agrees with the value given in Ref. [7], but it is a factor of 2 smaller than the value given in Ref. [8]. Note that the resonance widths given in Refs. [7,8] are obtained from the same experiment, although the fit of the data is obviously different. This fact emphasizes that not too much confidence should be placed on the comparison in Table II between the computed and experimental widths.

Aside from the two lowest  $2^+$  (bound and resonance) states, also a  $2_3^+$  state appears in the calculations. As seen in Table II, when the energy of the  $2_2^+$  resonance is moved from  $\sim 1.8$  to  $\sim 2.4$  MeV, the effect on the  $2_3^+$  state depends rather strongly on the potential used. With the Ali-Bodmer potential the energy moves from 3.90 to 6.87 MeV, and the width changes quite dramatically from a rather small value, 0.16 MeV, to 2.01 MeV. However, with the Buck potential basically only the resonance width changes, from 0.6 to 3.6 MeV, while the energy value

remains quite stable, since it only changes from 5.04 to 5.48 MeV.

Concerning the  $4^+$  states, the existence of a resonance at 6.81 MeV above the three-body threshold, with a width of 0.258 MeV has been known for a long time (Ref. [4]). Much more recently, an additional  $4^+$  state has been reported with an energy of 6.0 MeV (above threshold) and a width of 1.7 MeV [15]. Our calculations are consistent with the existence of a well-defined and relatively narrow resonance, which by means of the three-body force can be made to appear at 6.81 MeV, in agreement with the experimental value for the  $4_2^+$  state. The computed width for this resonance is 0.62 MeV with the Ali-Bodmer potential and 0.80 MeV with the Buck potential. When this is done it can be seen that a quite broad resonance ( $\sim 3.7$  MeV wide) appears numerically with both potentials at an energy of about  $\sim 5.4$  MeV. This broad resonance can be interpreted as the one given experimentally in Ref. [15]. Also, both the Ali-Bodmer and Buck potentials, give rise to a  $4_3^+$  state at 13.1 MeV, having also a similar width in the vicinity of 2.0 MeV.

As seen in Table II, the energies and widths of the resonances are rather independent of the choice made for the potential. In general, with the two potentials used, a similar three-body force gives rise to pretty much the same resonance properties. However, there are a few exceptions, mainly the  $0_3^+$  and  $2_3^+$  states, and the narrow  $2_2^+$  resonance at 1.7 MeV, which with the Ali-Bodmer potential is more than a factor of 2 broader than with the Buck potential. These differences can lead to visible differences in the differential cross sections, and therefore also in the transition strengths, for the cases where these potential-dependent resonances are involved.

As an illustration of how the resonance properties have been obtained, we show now in Fig. 1 the discretized continuum spectra after a complex scaling calculation for the  $0^+$  [Fig. 1(a)],  $2^+$  [Fig. 1(b)], and  $4^+$  [Fig. 1(c)] states in  $^{12}\text{C}$ . We show only the results obtained with the Buck potential. The

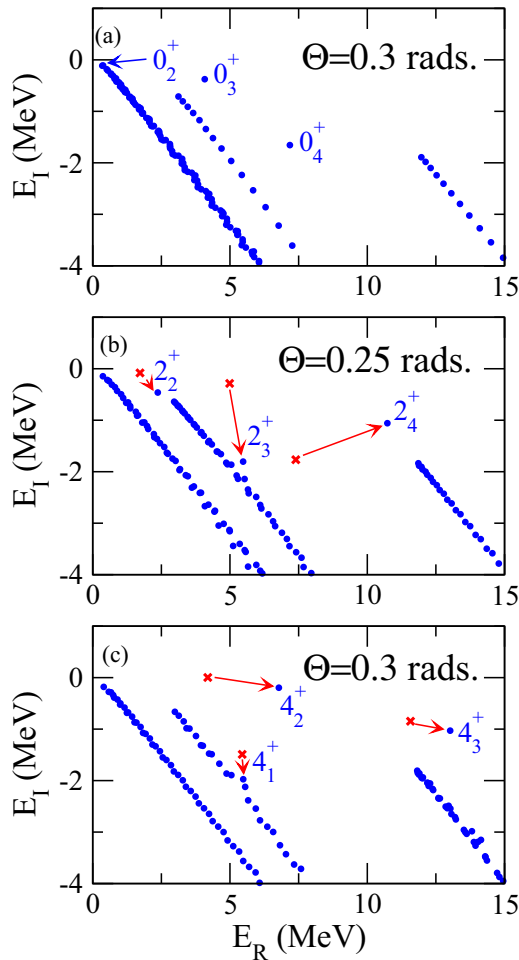


FIG. 1. (Color online) Fourth quadrant of the energy plane showing the discrete  $0^+$ ,  $2^+$ , and  $4^+$  continuum spectra in  $^{12}\text{C}$  after a complex scaling calculation with the Buck potential. The angle  $\theta$  on each panel is the scaling angle used in the corresponding calculation. The strength of the three-body force is  $-18.0$ ,  $-3.0$ , and  $13.4$  MeV for the  $0^+$ ,  $2^+$ , and  $4^+$  states, respectively. The bound  $0_1^+$  and  $2_1^+$  states are not shown. The lowest resonances for each of the three angular momenta are indicated by the corresponding labels. In the  $2^+$  and  $4^+$  cases the red crosses indicate the position of the resonances when the strength of the three-body force is reduced from  $-3.0$  to  $-12.1$  MeV, and from  $13.4$  to  $7$  MeV, respectively, and the arrows show how the resonances move when decreasing the three-body attraction.

calculations have been done using a complex scaling angle  $\theta$  of  $0.30$  rad for the  $0^+$  and  $4^+$  states, and  $0.25$  rad for the  $2^+$  states. In all the three cases, the energy cuts starting from the origin, from the  $2^+$  resonance in  $^8\text{Be}$ , and from the  $4^+$  resonance in  $^8\text{Be}$  are clearly seen. Note that, due to the very small energy of the  $0^+$  resonance in  $^8\text{Be}$ , the energy cut starting from the  $0^+$  state overlaps with the cut starting from the origin, which corresponds to strict three-body continuum states.

These cuts are rotated in the complex energy plane by an angle  $2\theta$ , and the states in the cuts correspond to pure continuum states. Typically, the states corresponding to the three-body resonances fall clearly out of the energy cuts, and their position is independent of the scaling angle  $\theta$ . These

resonances are indicated in the figure with the corresponding labels (the bound  $0_1^+$  and  $2_1^+$  states are not shown in the figure). However, there are several cases where the resonances lie pretty close to the continuum states, and their identification is not so obvious. The natural way to isolate these resonances from the continuum states would be to increase the value of the scaling angle  $\theta$ . However, this is not always an efficient solution due to the technical difficulties arising from the use of a too large scaling angle. For narrow resonances close to the threshold, such as the Hoyle state ( $0_2^+$  state), the resonance wave function falls exponentially to zero very fast, and the resonance can easily be identified by looking directly into the resonance wave function. For not very narrow resonances, such as the  $2_3^+$  state in Fig. 1(b), or the  $4_1^+$  in Fig. 1(c), it is much more efficient to separate the resonance from the continuum states by increasing the attraction of the three-body force, and trace how the resonance moves when the attraction of the three-body force is progressively released to the desired value. This is illustrated in Figs. 1(b) and 1(c), where the red crosses indicate the position of the resonances when the strength of the three-body force is put equal to  $-12.1$  MeV in the  $2^+$  case and  $7$  MeV in the  $4^+$  case. The red arrows show how the resonances move when decreasing the attraction. Using this procedure, the  $2_3^+$  and  $4_1^+$  resonances can be unambiguously identified.

It is interesting to note that the states denoted as  $4_1^+$  and  $4_2^+$  in Fig. 1(c) do actually cross when decreasing the repulsion of the three-body force (red crosses in the figure), in such a way that eventually, for a sufficiently large three-body attraction, the narrow resonance becomes the first  $4^+$  state and the broad one becomes the second  $4^+$  state. In other words, when decreasing the repulsion of the three-body force, the state denoted in Fig. 1(c) as  $4_2^+$  appears closer to the threshold than the  $4_1^+$  state. It is important to keep this fact in mind in order to determine which of the two first  $4^+$  states should be assigned to the first  $^{12}\text{C}$  band, and which one to the second.

### C. $^{12}\text{C}$ radii

In order to get a feeling of the size of the states, we show in Table III the expectation value  $\langle \rho^2 \rangle^{1/2}$  for the same cases shown in Table II. This expectation value will be denoted as  $\rho_{\text{rms}}$ , and it is computed within the complex scaling frame, meaning that  $\rho_{\text{rms}}^2 = \langle \Psi | \rho^2 e^{i2\theta} | \Psi \rangle$ , where  $\Psi$  is the complex rotated wave function of the resonance and  $\theta$  is the complex scaling angle used in the calculation [10]. Therefore, the expectation value is not necessarily real even though the  $\rho$  coordinate is. With this value it is possible to obtain the root mean square radius of each state ( $r_{\text{rms}}$  in Table III), which is given by

$$r_{\text{rms}}^2 = \frac{1}{12} \langle \Psi | \rho^2 | \Psi \rangle e^{i2\theta} + R_\alpha^2, \quad (18)$$

where  $R_\alpha = 1.47$  fm is the root mean square radius of the  $\alpha$  particle. Again, due to the complex scaling calculation, the computed  $r_{\text{rms}}$  of a resonance is in general a complex number. As discussed in Ref. [33], the imaginary part of a computed observable (the energy is the most obvious example) can be attempted interpreted as the uncertainty of the value given by



TABLE III. Computed values of  $\rho_{\text{rms}} = \langle \rho^2 \rangle^{1/2}$  (in fm) and  $r_{\text{rms}}$  (in fm) for the same  $^{12}\text{C}$  states shown in Table II.

$J^\pi$	$\rho_{\text{rms}}$ (AB)	$r_{\text{rms}}$ (AB)	$\rho_{\text{rms}}$ (Buck)	$r_{\text{rms}}$ (Buck)
$0_1^+$	6.9	2.5	6.8	2.5
$0_2^+$	11.5	3.6	11.4	3.6
$0_3^+$	$11.3 + i4.0$	$3.5 + i1.1$	$10.9 + i2.3$	$3.4 + i0.6$
$2_1^+$	6.8	2.5	6.7	2.4
$2_2^+$	$9.8 + i3.9/10.7 + i2.4$	$3.2 + i1.0/3.6 + i0.7$	$9.9 + i2.9/10.0 + i2.6$	$3.2 + i0.7/3.2 + i0.7$
$2_3^+$	$6.0 + i3.1/6.9 + i0.9$	$2.2 + i0.7/2.5 + i0.2$	$8.3 + i1.0/7.5 + i6.8$	$2.8 + i0.2/2.4 + i1.7$
$4_1^+$	$9.3 + i1.7$	$3.1 + i0.4$	$9.5 + i1.6$	$3.1 + i0.4$
$4_2^+$	$6.0 + i0.1$	$2.3 + i0.1$	$5.9 + i0.1$	$2.3 + i0.1$
$4_3^+$	$7.7 + i1.6$	$2.7 + i0.4$	$7.9 + i1.5$	$2.7 + i0.4$

the real part. This quantity permits a fast comparison between the spatial extensions of the different states.

As seen in the table, the results obtained with the Ali-Bodmer and Buck potentials are very similar. It is remarkable that, on the one side, the  $0_1^+$  and  $2_1^+$  states have similar sizes, both of them in the vicinity of  $\rho_{\text{rms}} \sim 6.8$  fm and  $r_{\text{rms}} \sim 2.5$  fm, and, on the other side, the same happens with the  $0_2^+$  and  $2_2^+$  resonances, with a value of  $\rho_{\text{rms}} \sim 10$  fm and  $r_{\text{rms}} \sim 3.4$  fm. This may suggest that these two sets of  $0^+$  and  $2^+$  states could correspond to two different rotational bands, each of them with a reasonably well-“frozen” structure. It is interesting to note that for the  $4_1^+$  and  $4_2^+$  states the computed values of  $\rho_{\text{rms}}$  are precisely about 10 and 6 fm, respectively, which might indicate a crossing of the first and second  $4^+$  states, in such a way that the  $4_1^+$  state could belong to the second band and the  $4_2^+$  state could belong to the first one. This is consistent with the discussion in Fig. 1(c), where we showed that the  $4_2^+$  state becomes actually the first  $4^+$  and the  $4_1^+$  state becomes the second  $4^+$  when the repulsion in the three-body force is diminished.

Finally, a third band could be present containing the  $0_3^+$ ,  $2_3^+$ , and  $4_3^+$  resonances. However, the values of  $\rho_{\text{rms}}$  given in Table III for these three states is not very stable (it ranges from 6.0 to 11.3 fm), and furthermore, as seen in Table II, the experimental energy of the  $0_3^+$  state is higher than the one of the  $2_3^+$  state, which makes it very unlikely that these two states belong to the same rotational band.

## V. ELECTRIC QUADRUPOLE CROSS SECTIONS

In this section we shall consider electric quadrupole cross sections for transitions between the different  $0^+$ ,  $2^+$ , and  $4^+$  states in  $^{12}\text{C}$ . These transitions involve bound states and resonances. As already mentioned, in this work we do not treat the resonances separately. We just compute the wave functions for the discrete continuum states obtained by imposing a box boundary condition. The only role of the resonance energies obtained in the previous section is to provide information about where to put the energy windows when computing the cross sections.

In general, the cross section, as a function of the incident energy, is given by Eq. (8), where the summation over  $j$  is restricted to the states within the chosen final energy window. For clean isolated resonance peaks it is easy to choose a meaningful, and rather well-defined, window around the peak. For

more complicated energy-dependent cross sections this could easily be more ambiguous. However, this would only reflect the more complicated physical nature resulting from overlapping and perhaps interfering resonances. Variation of choices of windows and subsequent analyses are then related to reduction of contributions to properties of individual resonances. Thus, the ambiguity in the choice of the window still remains but now containing information about the underlying physics

We shall here define the windows as  $E_R \pm \Gamma_R$ , where  $E_R$  and  $\Gamma_R$  are the energy and the width of the resonance in the initial or final state (we shall use the computed energies and widths given in Table II). Obviously, when the final state is a bound state the corresponding width is zero, and the summation over  $j$  in Eq. (8) disappears and the wave function in the right part of the matrix element refers to the bound-state wave function.

The continuum states have been discretized by imposing a box boundary condition to the radial solutions  $f_n(\rho)$  in the set of Eqs. (11). In particular, a box size of 200 fm has been used, which amounts to an average energy separation of about 0.03 MeV between the lower-lying continuum states. This means that for an energy window with a width in the scale of MeV we will have a significant amount of discrete continuum states within the final energy window. However, this procedure can not be applied to transitions into the Hoyle state. This resonance is extremely narrow (about 8 eV), which implies that only a huge box could provide a significant number of discrete continuum states within a final energy window of only a few eV wide.

Discretization of the continuum by use of such a huge box of perhaps 30000 fm compared to the 200 fm used in this work is clearly meaningless within the present numerical approach. The reasons are the huge number of necessary partial waves, the increasing basis size for each of the corresponding components, and the coupling of all the potentials due to the long-range Coulomb force. Therefore, the transitions into the Hoyle state will be treated as ordinary transitions into a bound state. On the other hand, this is a very accurate approximation for such a small width.

### A. $2^+ \rightarrow 0^+$ transitions

In Fig. 2, we show the cross section for the  $\alpha + \alpha + \alpha \rightarrow ^{12}\text{C} + \gamma$  reaction for a transition between the continuum  $2^+$  states and the ground state in  $^{12}\text{C}$ . The three-body force for

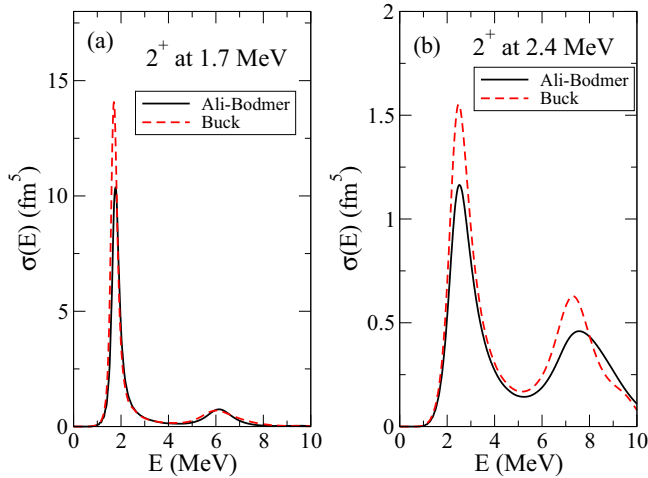


FIG. 2. (Color online) Cross section [Eq. (8)] for the  $2^+ \rightarrow 0_1^+$  transition in the  $\alpha + \alpha + \alpha \rightarrow {}^{12}\text{C} + \gamma$  reaction as a function of the three-body energy. The results with the Ali-Bodmer potential (solid curves) and the Buck potential (dashed curves) are shown. The (a) and (b) panels correspond to the calculations placing the  $2^+$  resonance at 1.7 and 2.4 MeV, respectively.

the  $0^+$  state has been chosen to reproduce the experimental separation energy of  ${}^{12}\text{C}$  into three alphas (see Table II). The figure shows the results obtained with the Ali-Bodmer potential (solid curves) and the Buck potential (dashed curves). Two different (structureless) three-body potentials have been used to place the  $2^+$  resonance at different energies.

In Fig. 2(a), the  $2^+$  energy is chosen to reproduce the measured binding energy of the bound  $2_1^+$  state. This implies that the first resonance  $2_2^+$  is found at about 1.7 MeV, which gives rise to the pronounced peak in the cross section around this energy. As we can see, the calculation using the Buck potential produces a taller peak than with the Ali-Bodmer potential. This is related to the fact that the computed  $2_2^+$  state is clearly narrower when the Buck potential is used. By fitting these peaks with the Breit-Wigner shape in Eq. (16), we extract the value of  $\Gamma_\gamma$  for the  $2_2^+ \rightarrow 0_1^+$  reaction, which for the Ali-Bodmer and Buck potentials is found to be 205 and 115 meV, respectively. We emphasize that, as seen from Eq. (16), in the center of the Breit-Wigner shape ( $E = E_R$ ) the value of the cross section is proportional to  $\Gamma_\gamma/\Gamma_R$  (assuming that  $\Gamma_\gamma \ll \Gamma_R$ ), and therefore different values of the cross section in the peak do not necessarily imply different values of the  $\Gamma_\gamma$  width, or, in other words, only for similar values of  $\Gamma_R$  the difference in the peaks of the cross section is directly translated into a difference in the  $\Gamma_\gamma$  values. The computed  $\Gamma_\gamma$  widths are collected in Table IV. Note that the presence of the  $2_3^+$  resonance at about 4 MeV with the Ali-Bodmer potential or 5 MeV with the Buck potential has no visible effect on the cross section. In fact, the small peak observed at around 6 MeV is basically produced by the broad  $2_4^+$  resonance, which with both potentials appears close to 6 MeV, as shown for the Buck potential by the red crosses in Fig. 1(b).

In the second calculation [Fig. 2(b)], the three-body force for the  $2^+$  states has been chosen such that the lowest  $2^+$  resonance is placed at about 2.4 MeV, in closer agreement

TABLE IV.  $\Gamma_\gamma$  widths, in meV, for the resonance-to-resonance transitions obtained after fitting the peaks in the cross sections for the different reactions with the Breit-Wigner shape given in Eq. (16). For the reactions where the  $2_2^+$  resonance enters, the two resonance energies, 1.7 and 2.4 MeV, have been considered.

$E_{2^+} =$	Ali-Bodmer		Buck	
	1.7 MeV	2.4 MeV	1.7 MeV	2.4 MeV
$2_2^+ \rightarrow 0_1^+$	205	160	115	175
$2_2^+ \rightarrow 0_2^+$	1.0	5.9	0.4	4.5
$2_3^+ \rightarrow 0_1^+$		1950		4300
$2_3^+ \rightarrow 0_2^+$	0.7	80	6.5	190
$2_2^+ \rightarrow 2_1^+$	6.4	22	4.0	22
$2_3^+ \rightarrow 2_1^+$	20	320	88	950
$4_1^+ \rightarrow 2_2^+$	130	44	118	57
$4_2^+ \rightarrow 2_2^+$	36	25	26	18
$4_1^+ \rightarrow 2_1^+$		50		50
$4_2^+ \rightarrow 2_1^+$		635		860
$4_3^+ \rightarrow 2_1^+$		3100		3500

to the experimental value given in Ref. [7]. The peaks in the cross sections are therefore shifted towards higher energies. As we can see, the new peaks are now clearly broader and almost a factor of 10 lower than before. Again, the calculation with the Buck potential gives rise to a taller peak than when the Ali-Bodmer potential is used. The  $\Gamma_\gamma$  widths obtained with the two potentials are in this case very similar, 160 and 175 meV, respectively. In this case, the second peak in the cross section located around 7 MeV is produced by the  $2_3^+$  resonance. From this peak we can also extract the  $\Gamma_\gamma$  widths for the  $2_3^+ \rightarrow 0_1^+$  reaction, which for completeness are also given in Table IV.

In Ref. [7], the  $\Gamma_\gamma$  width of the  $2_2^+$  resonance in  ${}^{12}\text{C}$  has been extracted from the photodissociation cross section of the  $0_1^+$  ground state, and it has been found to be  $60 \pm 10$  meV, which is roughly a factor of 3 smaller than the values obtained in this work when the  $2^+$  resonance is placed at 2.4 MeV (which is the energy that agrees better with the one given in the same reference). In Ref. [8], where the same experiment is analyzed, the  $\Gamma_\gamma$  width of the  $2_2^+$  state is quoted to be  $135 \pm 14$  meV, which agrees better with the results of our computation. However, as mentioned above, the relevant quantity when fitting the data with a Breit-Wigner shape is  $\Gamma_\gamma/\Gamma_R$ , which in both, Refs. [7,8], is of about  $6.5 \times 10^{-8}$ . This value is roughly a factor of 3 smaller than the value we have obtained with the  $2_2^+$  resonance at about 2.4 MeV ( $\Gamma_\gamma/\Gamma_R \approx 17 \times 10^{-8}$ ). Therefore, the photodissociation cross section for the  ${}^{12}\text{C} + \gamma \rightarrow \alpha + \alpha + \alpha$  shown in Refs. [7,8] should also be roughly a factor of 3 smaller than the one obtained in this work.

The photodissociation cross section can be extracted from the cross sections shown in Fig. 2 simply by using the relation in Eq. (4). The result is shown in Fig. 3, where the experimental data (multiplied by a factor of 3) are the ones given in Refs. [7] (squares) and [8] (circles) and the curves are our calculations with the Buck and Ali-Bodmer potentials (and the energy of the  $2_2^+$  resonance at about 2.4 MeV). As we can see, the shape of the experimental cross section is well reproduced. The

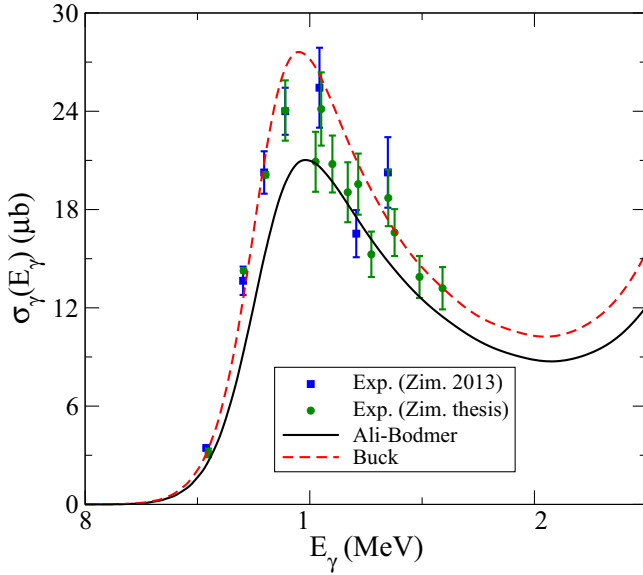


FIG. 3. (Color online) Photodissociation cross section for the  $^{12}\text{C} + \gamma \rightarrow \alpha + \alpha + \alpha$  reaction between the  $0^+$  ground state and the continuum  $2^+$  states as a function of the photon energy. The experimental curve has been multiplied by a factor of 3. The experimental data are from Refs. [7] (squares) and [8] (circles). Only the results with the  $2^+$  resonance at 2.4 MeV are shown for both, the Ali-Bodmer (solid) and Buck (dashed) potentials.

disagreement on the absolute value of the cross section may be related to the fact that only a fraction of the  $0^+$  ground state in  $^{12}\text{C}$  corresponds to the three-alpha structure used in this work. Another possibility is that improvements of the experimental analyses with the available conflicting results [7,8] also would change the normalization.

In Fig. 4 we show the same as in Fig. 2 for transitions from the  $2^+$  continuum states in  $^{12}\text{C}$  into the Hoyle state (treated as a bound state). Again, Figs. 4(a) and 4(b) show the result when the  $2^+$  resonance is at 1.7 and 2.4 MeV, respectively. The computed cross sections are clearly smaller than for transitions

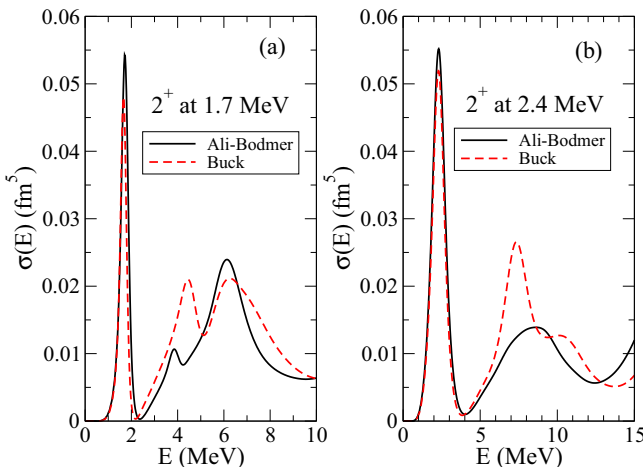


FIG. 4. (Color online) The same as Fig. 2 for the  $2^+ \rightarrow 0^+$  transition in the  $\alpha + \alpha + \alpha \rightarrow ^{12}\text{C} + \gamma$  reaction.

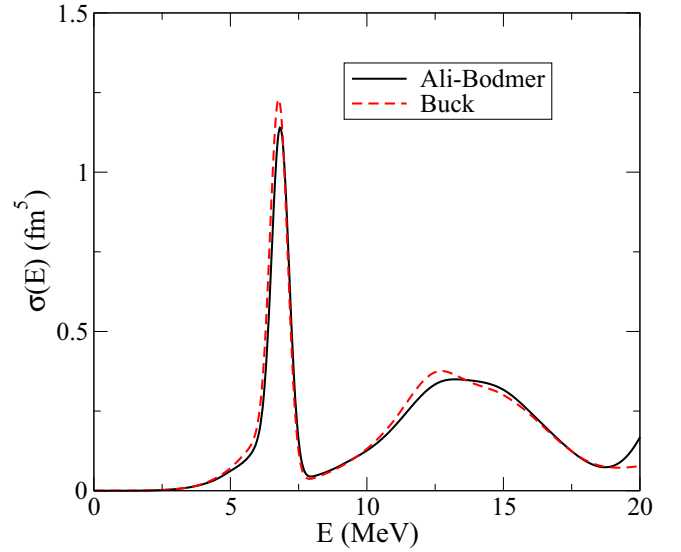


FIG. 5. (Color online) The same as Fig. 2 for the  $4^+ \rightarrow 2^+$  transition in the  $\alpha + \alpha + \alpha \rightarrow ^{12}\text{C} + \gamma$  reaction.

into the  $0^+$  ground state. Together with the main peak produced by the  $2^+$  resonance, several other peaks produced by higher  $2^+$  states are clearly seen. In particular, in Fig. 4(a) a small peak can be seen at an energy of around 4 MeV for the Ali-Bodmer potential and 5 MeV for the Buck potential. These two peaks are produced by the  $2^+$  resonance given in Table II. An additional peak produced by the  $2^+$  resonance at about 6 MeV is also seen in the cross section. The computed  $\Gamma_\gamma$  widths obtained after fitting the lower peak in Fig. 4(a) with the Breit-Wigner shape in Eq. (16) are 1.0 and 0.4 meV with the Ali-Bodmer and Buck potentials, respectively.

When the  $2^+$  resonance is at 2.4 MeV [Fig. 4(b)] the  $2^+$  state becomes very broad and moves up in energy, giving rise to the corresponding bumps in the cross section observed in Fig. 4(b). In the case of the Buck potential a bump produced by the  $2^+$  state at about 11 MeV [Fig. 1(b)] is also seen. The computed  $\Gamma_\gamma$  widths for the transition from the  $2^+$  state to the Hoyle state are in this case 5.9 and 4.5 meV with the Ali-Bodmer and the Buck potentials, respectively. For completeness, we also give in Table IV the computed values of  $\Gamma_\gamma$  for the  $2^+ \rightarrow 0^+$  transition.

### B. $4^+ \rightarrow 2^+$ transitions

In Fig. 5 we show the cross section for the  $4^+ \rightarrow 2^+$  transition. The three-body force in the  $2^+$  states is such that the binding energy of the  $2^+$  bound state matches the experimental value. The two potentials, Ali-Bodmer and Buck, give very similar results with a very sharp peak at 6.8 MeV, which is actually produced by the  $4^+$  resonance. The effect of the broad  $4^+$  state can be seen in the little shoulder that appears in the cross section around 5 MeV. This is more clearly seen in Fig. 6, where we fit for the Ali-Bodmer [Fig. 6(a)] and Buck [Fig. 6(b)] potentials the cross section peak as a linear combination of two Breit-Wigner functions with the parameters for the  $4^+$  (dashed curves) and  $4^+$

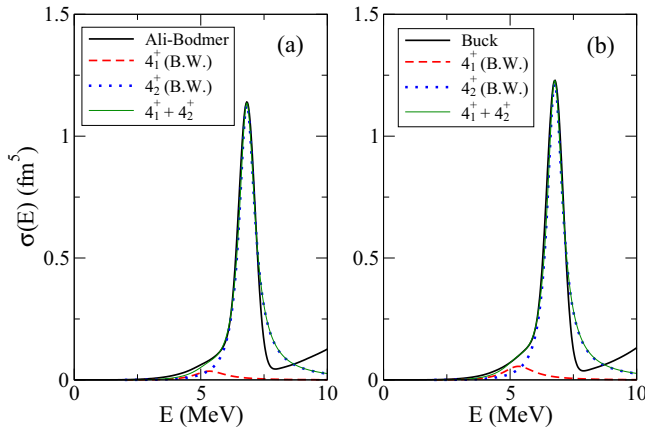


FIG. 6. (Color online) Fit of the sharp peak in the cross section for the  $4^+ \rightarrow 2_1^+$  transition by means of two Breit-Wigner functions with the parameters corresponding to the  $4_1^+$  and  $4_2^+$  resonances given in Table II. Panels (a) and (b) show the fit when the Ali-Bodmer and Buck potentials, respectively, are used. The thick-solid curve is the computed cross section as shown in Fig. 5. The dashed and dotted curves are the Breit-Wigner functions corresponding to the  $4_1^+$  and  $4_2^+$  resonances, respectively, whose sum is shown by the thin-solid curve.

(dotted curves) resonances given in Table II. The sum of the two Breit-Wigner curves is shown by the thin-solid curves, which match pretty well the peak of the computed cross sections (thick-solid curves). The coefficients in this linear combination give directly the  $\Gamma_\gamma$  widths for the  $4_1^+ \rightarrow 2_1^+$  and  $4_2^+ \rightarrow 2_1^+$  transitions, which are, with the Ali-Bodmer and Buck potentials, 50 and 80 meV for the first transition, and 635 and 855 meV for the second transition, respectively. The broad peak observed at about 13 MeV is mainly produced by the  $4_3^+$  resonance, which has very similar properties with the two potentials. The  $\Gamma_\gamma$  values for the  $4_3^+ \rightarrow 2_1^+$  transitions are also given in Table IV.

In Fig. 7 we show the cross sections for the  $4^+ \rightarrow 2_2^+$  transitions. Again, two possible energies, 1.7 and 2.4 MeV, have been considered for the  $2_2^+$  resonance [Figs. 7(a) and 7(b), respectively]. This is a transition into a resonant state, which implies that the summation over  $j$  in Eq. (8) is made over the discrete continuum final states within the energy window  $E_R \pm \Gamma_R$ , where  $E_R$  and  $\Gamma_R$  are the energy and width of the final resonance. Therefore, the value of the cross section will be fully determined by the arbitrary choice for the width of the final energy window.

The calculation of the continuum-to-continuum cross section presents also the numerical complication of the so-called infrared catastrophe (see Ref. [19]), which appears in the region of small  $E_\gamma$  values ( $E$  close to  $E'$ ) due to the  $1/E_\gamma$  dependence of the bremsstrahlung cross section at small photon energies. Therefore, the cross sections shown in Fig. 7 by the thick-solid (Ali-Bodmer) and thick-dashed (Buck) curves will be contaminated by this effect, also called soft-photon contribution, for initial energies ( $E$ ) in the vicinity of the final energy window [centered at  $\sim 1.75$  MeV in Fig. 7(a) and at  $\sim 2.4$  MeV in panel 7(b)]. A fully relativistic

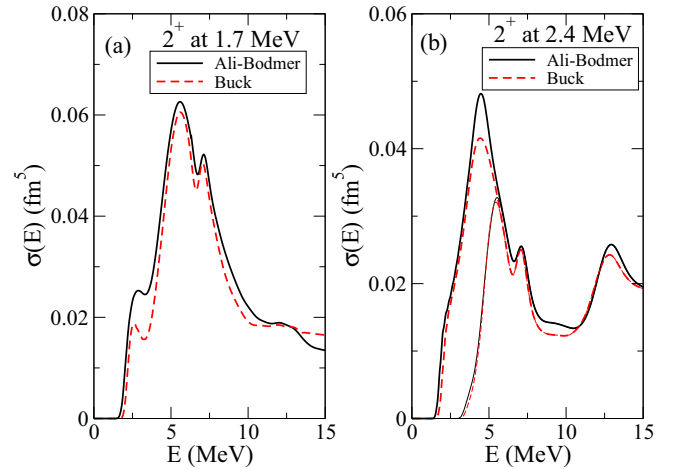


FIG. 7. (Color online) The same as Fig. 2 for the  $4^+ \rightarrow 2_2^+$  transition in the  $\alpha + \alpha + \alpha \rightarrow {}^{12}\text{C} + \gamma$  reaction. In panel (b) the thin-solid and thin-dashed curves are the cross sections for the Ali-Bodmer and Buck potentials, respectively, using a cutoff for the photon energy of 2 MeV.

treatment of the bremsstrahlung cross section would correct this anomaly [39].

In Fig. 7(a) the effect of the soft-photon contribution is seen in the little shoulder observed at about 2 MeV. This peak is therefore unphysical and it does not correspond to any resonance in the initial state. The other two peaks, at about 5.5 and 7.2 MeV, correspond to the  $4_1^+$  and  $4_2^+$  states, although the large width of the  $4_1^+$  resonance gives rise to a large interference between the two lowest  $4^+$  states.

In the case shown in Fig. 7(b) ( $2_2^+$  resonance at  $\sim 2.4$  MeV) the final energy window reaches a value of around 3.5 MeV. For this reason the soft-photon peak and the one corresponding to the broad  $4_1^+$  resonance can not be distinguished in this case. Usually the soft-photon contribution is removed by introducing a cutoff in the photon energy. In Fig. 7(b) the thin-solid and thin-dashed curves are the cross sections with the Ali-Bodmer and Buck potentials, respectively, when a cutoff of 2 MeV is used for  $E_\gamma$ . This cutoff has been chosen in order to place the  $4_1^+$  peak at an energy of  $\sim 5.5$  MeV, similar to the one observed in Fig. 7(a), that we know from the value of the  $4_1^+$  energy should be the correct position. Although the choice of the cutoff value is to some extent arbitrary, it should not be much bigger than 2 MeV since the energy separation between the  $4_1^+$  and the  $2_2^+$  resonances in Fig. 7(b) is of about 3 MeV. For this reason, the transition strengths obtained from the lowest peak in Fig. 7(b) (thin curves) for the  $4_1^+ \rightarrow 2_2^+$  process should be taken as a minimum value. A choice of the cutoff energy smaller than 2 MeV would increase the strength. The second peak at  $\sim 7.1$  MeV is produced by the  $4_2^+$  state. The position and height of this peak are not affected by the cutoff in the photon energy, but, again, it contains an important interference from the  $4_1^+$  resonance.

In order to extract the  $\Gamma_\gamma$  values for the  $4_1^+ \rightarrow 2_2^+$  and  $4_2^+ \rightarrow 2_2^+$  transitions, and due to the large interference between the two lowest  $4^+$  resonances, it is convenient to proceed as discussed in Fig. 6, and make a simultaneous fit of the  $4_1^+$  and



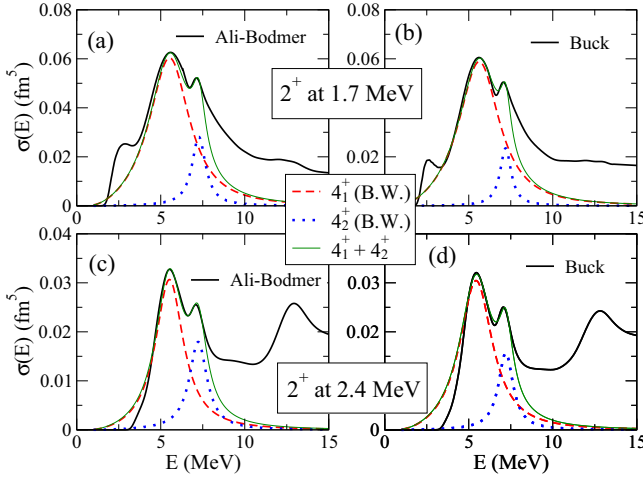


FIG. 8. (Color online) Fit of the cross section for the  $4^+ \rightarrow 2^+$  transition by means of two Breit-Wigner functions with the parameters corresponding to the  $4_1^+$  and  $4_2^+$  resonances given in Table II. Panels (a) and (b) show the fit when the Ali-Bodmer and Buck potentials, respectively, are used and the  $2^+$  resonance is found at 1.7 MeV. Panels (c) and (d) show the same as (a) and (b) when the  $2^+$  resonance energy is 2.4 MeV. The thick-solid curve is the computed cross section as shown in Fig. 7 [with the photon energy cutoff in panels (c) and (d)]. The dashed and dotted curves are the Breit-Wigner functions corresponding to the  $4_1^+$  and  $4_2^+$  resonances, respectively, whose sum is shown by the thin-solid curve.

$4_2^+$  peaks in the cross sections by means of Eq. (16). These fits are shown in Fig. 8. Figures 8(a) and 8(b) are the calculations with the Ali-Bodmer and Buck potentials for the  $2^+$  state at 1.7 MeV, and Figs. 8(c) and 8(d) are the same calculations with the  $2^+$  state at 2.4 MeV. In these two last panels the fit has been made to the cross sections obtained after removing the soft-photon contribution by means of the cutoff in  $E_\gamma$  [thin curves in Fig. 7(b)]. The Breit-Wigner curves corresponding to the  $4_1^+$  and  $4_2^+$  states are shown by the dashed and dotted curves, respectively, and they have been obtained using  $\Gamma_\gamma$  values equal to 130 and 36 meV, respectively, in Fig. 8(a), 118 and 26 meV in Fig. 8(b), 44 and 25 meV in Fig. 8(c), and 57 and 18 meV in Fig. 8(d). The sum of the two Breit-Wigner fits is given by the thin-solid curves, which clearly disagree with the computed total cross section (thick-solid curves) for large energies. This is due to the fact neither the contribution from the wide  $4_3^+$  state given in Table II nor the contribution from the continuum background have been included in fit.

Finally, we show in Fig. 9 the corresponding cross sections for the  $2^+ \rightarrow 2_1^+$  transitions. The peaks produced by the  $2_2^+$  and  $2_3^+$  resonances are clearly seen in all the cases. The  $\Gamma_\gamma$  widths for the  $2_2^+ \rightarrow 2_1^+$  and  $2_3^+ \rightarrow 2_1^+$  transitions with the two potentials and the two different energies of the  $2_2^+$  resonance considered in this work are again given in Table IV.

## VI. $\mathcal{B}(E2)$ TRANSITION STRENGTHS

The photoemission processes from a bound state into other bound states or into the continuum is described unambiguously by the transition strength. This is not true any more for

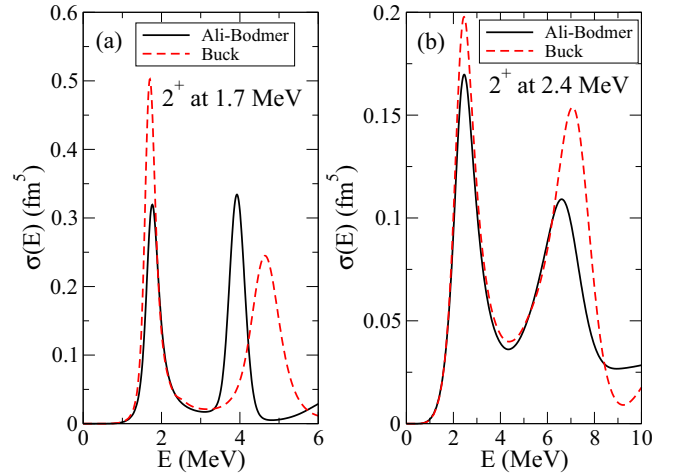


FIG. 9. (Color online) The same as Fig. 2 for the  $2^+ \rightarrow 2_1^+$  transition in the  $\alpha + \alpha + \alpha \rightarrow {}^{12}\text{C} + \gamma$  reaction.

continuum-to-continuum transitions even when rather well-defined resonance peaks are present in the corresponding cross sections. These transition strengths are decisive indicators for structure similarities between excited states, where prominent examples are collective rotational or vibrational states built on the same intrinsic configuration. In our present case of three alpha particles, such collective rotations have been suggested many times. This necessarily involves continuum structures with all the related ambiguities. Still, we want to know if collective rotations are a reasonable description of some of the states in the  ${}^{12}\text{C}$  spectrum. We therefore first discuss the detailed numerical results from our three-body model, and in the following subsection we relate to the simplest possible rotational model.

### A. Numerical results

In Sec. III C we described the two methods used in this work to extract the transition strength for reactions involving continuum states. In the first method we integrate the cross section [Eq. (7)] over two energy windows chosen around the initial and final resonance energies. In this work we have taken the windows as  $E_R \pm \Gamma_R$  where  $\Gamma_R$  is the width of the resonance. This procedure is equivalent to integration of the cross sections computed in the previous section over the initial energy  $E$  under the peaks corresponding to the initial resonant state. The total cross section obtained in this way is divided by the constants multiplying the transition strength [see Eqs. (5) and (7)]. These transition strengths will be denoted by  $\mathcal{B}_\sigma$ . The application of this method requires well-separated peaks in the cross sections for each of the resonances, in such a way that the integration under a given peak contains very little contamination from the interference with other states. However, this is not always the case in our calculations. In particular, the  $4_1^+$  and  $4_2^+$  states are very close to each other, giving rise to a large interference between them, as seen in Figs. 6 and 8. For this reason, for transitions having the  $4_1^+$  or  $4_2^+$  resonances as initial state, the integration of the cross section over the initial energy window will be made

considering not the computed cross section (thick solid curves in Figs. 6 and 8), but the Breit-Wigner curves corresponding to each of the resonances (dashed curves for the  $4_1^+$  state and dotted curve for the  $4_2^+$  state). In the second method we make use of Eq. (17), where  $\Gamma_\gamma$  has been extracted after fitting the computed cross section with the Breit-Wigner shape in Eq. (16). The values of  $\Gamma_\gamma$  have been given in Table IV. The transition strengths computed in this way will be denoted by  $\mathcal{B}_\gamma$ .

The first two lines in Table V show the computed strengths for the  $2_1^+ \rightarrow 0_1^+$  and  $4_2^+ \rightarrow 2_1^+$  transitions, which are tempting to associate with transitions between states belonging to the first rotational band in  $^{12}\text{C}$ . In here we have taken into account that, as suggested by the computed values of  $\rho_{\text{rms}}$  (see Table III) and the behavior of the  $4_1^+$  and  $4_2^+$  resonances when modifying the three-body force (Fig. 1), the  $4_2^+$  state is expected to belong to the first band and the  $4_1^+$  state to the second. The first transition in the table involves only bound states, and the results obtained with the Ali-Bodmer and Buck potentials are similar,  $10.2 e^2\text{fm}^4$  and  $9.9 e^2\text{fm}^4$  which are in good agreement with the result in Ref. [12] from a microscopic  $\alpha$ -cluster model calculation. These values are a bit bigger than the one obtained in Ref. [14] where the microscopic antisymmetrized molecular dynamics (AMD) method was used. The results are also bigger than the experimental value [12] which most temptingly can be attributed to a better match between the  $3\alpha$  wave functions than nature prescribes.

For the  $4_2^+ \rightarrow 2_1^+$  transition the computed  $\mathcal{B}_\gamma$  strengths agree slightly better with the AMD calculation than the  $\mathcal{B}_\sigma$  values, which are a bit smaller. In comparison to other model calculations it is important to know the conceptual difference between our continuum calculation and these bound-state treatments. When a resonance is located in the continuum with a substantial width, it is very likely that the transition strength is reduced due to a smaller overlap of wave functions than by assuming one bound-state-like resonance wave function. It is also important to keep in mind that the choice of the energy windows when computing  $\mathcal{B}_\sigma$  is arbitrary, and a small increase in such windows will give rise to values of  $\mathcal{B}_\sigma$  closer to  $\mathcal{B}_\gamma$ .

The next two lines in the table give the  $E2$ -transition strengths between the states in the second sequence of energies, i.e., the  $2_2^+ \rightarrow 0_2^+$  and  $4_1^+ \rightarrow 2_2^+$  transitions. In order to see the dependence on the energy of the  $2_2^+$  resonance, we show, as in Table IV, the results corresponding to a  $2_2^+$  energy of 1.7 and 2.4 MeV.

For the  $2_2^+ \rightarrow 0_2^+$  transition, when the  $2_2^+$  resonance is at 1.7 MeV, the results with the Buck potential are clearly smaller than the values obtained with the Ali-Bodmer potential. This is particularly true for  $\mathcal{B}_\gamma$ , where the difference is of almost a factor of 2. This is due to the fact that the width of the  $2_2^+$  resonance (at 1.7 MeV) with the Buck potential is around half the width of the one with the Ali-Bodmer potential (see Table II). As seen in Fig. 4(a), the height of the cross section peak corresponding to this resonance is similar for both potentials. This implies that  $\Gamma_\gamma/\Gamma_R$  is also similar in both cases. Therefore, a  $\Gamma_R$  value about a factor of 2 smaller gives rise to a  $\Gamma_\gamma$  value also about a factor of 2 smaller, and consequently, as seen in Eq. (16), a transition strength also about a factor of 2 smaller. For a  $2_2^+$  energy of 2.4 MeV, which

is in better agreement with the experimental value given in Refs. [7,8], the computed strengths with the Ali-Bodmer and Buck potentials are now closer to each other (the difference between the corresponding  $\Gamma_R$  values is now small). Also, the  $\mathcal{B}_\gamma$  and  $\mathcal{B}_\sigma$  values are reasonably consistent with each other, and they are clearly bigger than the AMD result ( $102 e^2\text{fm}^4$ ) given in Ref. [14]. In any case, this difference is relatively unimportant compared to the sensitivity of the computed transition strengths on the methods used.

For the  $4_1^+ \rightarrow 2_2^+$  transition the results obtained with the two potentials are consistent with each other, even if  $\mathcal{B}_\gamma$  changes from 153 to 220  $e^2\text{fm}^4$  when the  $2_2^+$  state is at 2.4 MeV. One has to take into account that, together with the inherent uncertainties in the determination of  $\mathcal{B}_\gamma$  and  $\mathcal{B}_\sigma$ , for reactions involving the  $4_1^+$  and  $4_2^+$  states we have to deal with the additional uncertainty arising from the interference between the two resonances and the soft-photon contribution. For this reason, the agreement between the  $\mathcal{B}_\gamma$  and  $\mathcal{B}_\sigma$  values seen in Table V for the  $4_1^+ \rightarrow 2_2^+$  reaction can be considered quite acceptable. In any case, all the results given in the table for this reaction are significantly smaller than the result given in Ref. [14].

In the lower part of Table V we show the computed transition strengths between states belonging to different bands. For the  $2_1^+ \rightarrow 0_2^+$  transition (where the Hoyle state is treated as a bound state) we obtain a strength of  $\sim 0.9 e^2\text{fm}^4$ , in reasonably good agreement with the result of the microscopic  $\alpha$ -cluster calculation given in Ref. [12], but clearly smaller than the experimental value. For the  $2_2^+ \rightarrow 0_1^+$  transition our computed strengths are quite stable, although the agreement with the microscopic  $\alpha$ -cluster calculation given in Ref. [12] is better, as expected, when the energy of the  $2_2^+$  resonance is put at about 2.4 MeV, also in better agreement with the experimental value. However, these energies of about 2 MeV are in clear disagreement with the AMD result. When compared to the experimental data, our strength is about a factor of 3 bigger than the result given in Ref. [7], but in better agreement with the value given in Ref. [8], where the same experiment as in Ref. [7] is reexamined (see Fig. 3). For the  $4_2^+ \rightarrow 2_2^+$  transition our results are reasonably consistent with the AMD calculation, especially when considering the  $\mathcal{B}_\gamma$  values. The computed strengths for the transitions  $4_1^+ \rightarrow 2_1^+$  and  $2_2^+ \rightarrow 2_1^+$  are also given, although for these cases the comparison with previous results or experimental data is not possible.

In general, the computed  $\mathcal{B}_\sigma$  and  $\mathcal{B}_\gamma$  strengths are consistent with each other, especially if we take into account that the computed  $\mathcal{B}_\sigma$  values are obviously dependent on the width chosen for the energy windows, and the  $\mathcal{B}_\gamma$  strengths are very sensitive to the value of  $E_\gamma$  used in Eq. (17) since the photon energy appears to the fifth power. This is particularly true when the initial and final energies are not very far from each other, like for instance in the  $2_2^+ \rightarrow 0_2^+$  transition with the  $2_2^+$  energy at 1.7 MeV. In this case a variation of  $E_\gamma$  from 1.3 to 1.4 MeV (and  $\Gamma_\gamma = 1$  meV) implies a change in  $\mathcal{B}_\gamma$  from 230 to 330  $e^2\text{fm}^4$ . Together with this, the results involving the  $4_1^+$  and  $4_2^+$  states have the additional uncertainty arising from the interference between them and the soft-photon contribution.

TABLE V.  $B(E2)$  transition strengths in  $e^2\text{fm}^4$  for different transitions between  $^{12}\text{C}$  states. For transitions from continuum states,  $B_\gamma$  and  $B_\sigma$  denote the strengths obtained from Eq. (17) and from the total (integrated) cross section, respectively. For the reactions involving the  $2_2^+$  resonance the two cases, with the resonance energy at 1.7 and 2.4 MeV, have been considered. The second, third, and fourth columns give the known experimental values, and the results obtained with the microscopic cluster model calculation described in Ref. [12] (labeled as  $\alpha$  cluster) and with the antisymmetrized molecular dynamics (AMD) method. The corresponding references are given in the table.

Transition	Expt.	$\alpha$ cluster	AMD	Ali-Bodmer	Buck
$2_1^+ \rightarrow 0_1^+$	$7.6 \pm 0.4^a$	$9.16^a$	$8.4^d$	10.2	9.9
$4_2^+ \rightarrow 2_1^+$			$15.8^d$		
$2_2^+ \rightarrow 0_1^+$			$102^d$	$B_\sigma = 8.2$ $E_{2^+} = 2.4 \text{ MeV}$	$B_\gamma = 12.5$ $E_{2^+} = 1.7 \text{ MeV}$
$4_1^+ \rightarrow 2_1^+$			$595^d$		
$2_1^+ \rightarrow 0_2^+$			$5.1^d$	0.91	0.96
$4_1^+ \rightarrow 2_1^+$	$2.6 \pm 0.4^a$	$0.84^a$			
$2_2^+ \rightarrow 0_1^+$	$0.73 \pm 0.13^b$ $1.57 \pm 0.13^c$	$1.99^a$	$0.4^d$	$B_\gamma$ 3.1 $B_\sigma$ 2.0	$B_\gamma = 1.2$ $E_{2^+} = 1.7 \text{ MeV}$ $B_\gamma$ 2.4 $B_\sigma$ 2.8
$2_2^+ \rightarrow 2_1^+$				$B_\gamma$ 2.9 $B_\sigma$ 4.0	$B_\gamma$ 2.5 $B_\sigma$ 2.9
$4_2^+ \rightarrow 2_2^+$			$7.5^d$	$B_\gamma$ 9.8 $B_\sigma$ 5.0	$B_\gamma$ 6.5 $B_\sigma$ 3.5

<sup>a</sup>Reference [12].

<sup>b</sup>Reference [7].

<sup>c</sup>Reference [8].

<sup>d</sup>Reference [14].

When comparing the results with the Ali-Bodmer and Buck potentials, the general conclusion is that there are no significant differences between them. Only in the transitions involving the  $2_2^+$  resonance at 1.7 MeV an important difference, mainly for the  $\mathcal{B}_\gamma$  values, has been observed. This is due to the very different width obtained for this resonance with each of the potentials. Therefore, from the transition strengths it is not possible to answer the question of what potential is more appropriate in order to describe the alpha-alpha interaction.

### B. Rotational model

For transitions between states within a schematic rotational band, and assuming axial symmetry for the system, the quadrupole transition strength is given by [40]

$$\mathcal{B}^{(E2)}(J \rightarrow J') = \frac{5}{16\pi} Q_0^2 \langle J0; 20 | J'0 \rangle^2, \quad (19)$$

where the projection  $K$  of the angular momentum on the intrinsic symmetry axis has been assumed to be zero. The intrinsic quadrupole moment  $Q_0$  is given by

$$Q_0 = \left\langle \sum_i q_i (2z_i^2 - x_i^2 - y_i^2) \right\rangle, \quad (20)$$

where  $i$  runs over all the charged particles with charge  $q_i$  and whose center of mass coordinates are denoted by  $(x_i, y_i, z_i)$ , where the  $z$  axis is chosen along the intrinsic symmetry axis. The expectation value is taken in the intrinsic body-fixed coordinate system. The quadrupole moment is a measure of the deformation and it has ideally one characteristic value for a sequence of states belonging to a given rotational band. From each of the calculated transition strengths given in Table V, it is then easy to obtain from Eq. (19) the absolute value of the intrinsic quadrupole moments. The  $|Q_0|$  values obtained in this way are given in Table VI.

The intrinsic quadrupole moment  $Q_0$  is related to the static quadrupole moment  $Q$  of each individual state with angular

momentum  $J$  by the simple expression

$$Q = \sqrt{\frac{16\pi}{5}} \langle JJ | \hat{O}_{20} | JJ \rangle = -\frac{J}{2J+3} Q_0, \quad (21)$$

where the operator  $\hat{O}_{\lambda\mu}$  is given in Eq. (3) and, again, a band with  $K = 0$  has been assumed.

For the transitions between the states in the first band  $2_1^+ \rightarrow 0_1^+$  and  $4_2^+ \rightarrow 2_1^+$  (the state  $4_2^+$  is the one assigned to the first band), the computed values of  $|Q_0|$  in Table VI are rather stable, consistent with each other, and consistent as well with the experimental value and previous calculations. The value of the static quadrupole moment  $Q$  can be easily computed for the bound  $2_1^+$  state, and we have obtained 6.6 and 6.5  $efm^2$  with the Ali-Bodmer and Buck potentials, respectively. These values agree with the experimental value of  $6 \pm 3 \text{ efm}^2$  given in Ref. [41]. From Eq. (21) we can then extract the intrinsic quadrupole moment for the  $2_1^+$  bound state, which is found to be  $-22.7$  and  $-23.0 \text{ efm}^2$  with the Ali-Bodmer and Buck potentials, respectively. This result agrees as well with the  $-21.6 \text{ efm}^2$  given in the Ref. [42]. These values are also consistent with the ones quoted in the first two rows in Table VI for the  $2_1^+ \rightarrow 0_1^+$  and  $4_2^+ \rightarrow 2_1^+$  transitions. These results support the idea of the states in this band as arising from the rotation of a given intrinsic state, and also the fact the  $4_2^+$  state is the one actually belonging to the first band.

For the transitions in the second band  $2_2^+ \rightarrow 0_2^+$  and  $4_1^+ \rightarrow 2_2^+$ , the relative difference between the computed values of  $|Q_0|$  is higher than the one found in the first band. Typically, the results for the  $4_1^+ \rightarrow 2_2^+$  transition are even 25% smaller than the ones for the  $2_2^+ \rightarrow 0_2^+$  transition. If we restrict ourselves to the results involving the  $2_2^+$  state at 2.4 MeV, which is in better agreement with the experimental value, the computed  $|Q_0|$  values range from  $\sim 70$  up to  $\sim 90 \text{ efm}^2$ . Taking into account all the uncertainties already discussed, especially when the  $4_1^+$  state is involved, we can consider that these results are consistent with each other. In this connection, it is important to remember that, as discussed in Fig. 7(b), the transition

TABLE VI. Absolute value of the intrinsic transition quadrupole moments  $|Q_0|$  (in  $efm^2$ ) obtained from the  $\mathcal{B}(E2)$  transition strengths given in Table V and Eq. (19).  $|Q_{0\sigma}|$  and  $|Q_{0\gamma}|$  denote the intrinsic quadrupole moments obtained from the transition strengths  $\mathcal{B}_\sigma$  and  $\mathcal{B}_\gamma$ , respectively.

Transition	Expt.	$\alpha$ cluster	AMD	Ali-Bodmer				Buck			
$2_1^+ \rightarrow 0_1^+$	$19.5 \pm 0.5$	21.46	20.5	22.6				22.3			
$4_2^+ \rightarrow 2_1^+$			23.6	$ Q_{0\gamma}  = 17.8$		$ Q_{0\sigma}  = 17.0$		$ Q_{0\gamma}  = 21.0$		$ Q_{0\sigma}  = 18.7$	
				$E_{2^+} = 1.7 \text{ MeV}$		$E_{2^+} = 2.4 \text{ MeV}$		$E_{2^+} = 1.7 \text{ MeV}$		$E_{2^+} = 2.4 \text{ MeV}$	
				$ Q_{0\gamma} $	$ Q_{0\sigma} $	$ Q_{0\gamma} $	$ Q_{0\sigma} $	$ Q_{0\gamma} $	$ Q_{0\sigma} $	$ Q_{0\gamma} $	$ Q_{0\sigma} $
$2_2^+ \rightarrow 0_2^+$			72	108	94	92	84	78	82	89	83
$4_1^+ \rightarrow 2_2^+$			145	77	69	73	68	73	68	88	71
$2_1^+ \rightarrow 0_2^+$	$11.4 \pm 0.9$	6.50	16.0	6.8				6.9			
$4_1^+ \rightarrow 2_1^+$				$ Q_{0\gamma}  = 6.5$		$ Q_{0\sigma}  = 4.6$		$ Q_{0\gamma}  = 6.5$		$ Q_{0\sigma}  = 5.9$	
				$E_{2^+} = 1.7 \text{ MeV}$		$E_{2^+} = 2.4 \text{ MeV}$		$E_{2^+} = 1.7 \text{ MeV}$		$E_{2^+} = 2.4 \text{ MeV}$	
				$ Q_{0\gamma} $	$ Q_{0\sigma} $	$ Q_{0\gamma} $	$ Q_{0\sigma} $	$ Q_{0\gamma} $	$ Q_{0\sigma} $	$ Q_{0\gamma} $	$ Q_{0\sigma} $
$2_2^+ \rightarrow 0_1^+$	$6.03 \pm 0.54$ $8.88 \pm 0.37$	10.0	4.5	14.3	12.5	10.0	9.8	11.0	11.9	10.8	10.5
$2_2^+ \rightarrow 2_1^+$				11.2	10.1	13.9	13.5	9.4	10.1	13.9	13.8
$4_2^+ \rightarrow 2_2^+$			16.2	17.3	11.9	18.6	13.3	15.1	11.1	16.2	12.9



strengths obtained from the  $4_1^+$  peak for the  $4_1^+ \rightarrow 2_2^+$  reaction should be taken as its minimum value. A small decrease in the photon energy cutoff would enhance the  $4_1^+$  peak in Fig. 7(b), making the strengths of the  $4_1^+ \rightarrow 2_2^+$  process closer to the ones of the  $2_2^+ \rightarrow 0_2^+$  reaction. Therefore, we can conclude that the transition strengths given in Table VI between the states in the second band in  $^{12}\text{C}$  are also consistent with the idea of a relatively well “frozen” structure and the rotational character of the band. For the same reason, we can also consider that our results are not dramatically far from the  $72 \text{ efm}^2$  and  $145 \text{ efm}^2$  obtained in Ref. [14].

In the lower part of Table VI we give the intrinsic quadrupole moments for the transitions between states in different bands. It is interesting to note that for the  $4_1^+ \rightarrow 2_1^+$  transition, which in principle should be a transition belonging to the first rotational band, we obtain a value for  $|Q_0|$  even a factor of 3 smaller than the values quoted in the upper part of the table for the  $2_1^+ \rightarrow 0_1^+$  and  $4_2^+ \rightarrow 2_1^+$  transitions. This result is then also consistent with the assignment of the  $4_2^+$  state to the first band and the  $4_1^+$  state to the second. In fact, as also seen in the table, the  $|Q_0|$  value for the  $4_2^+ \rightarrow 2_2^+$  is also clearly smaller than the values for the transitions between the states in the second band.

A different approach can be made by applying the definition given in Eq. (20) to a system made of three pointlike  $\alpha$  particles in a schematic triangular structure, as shown in Fig. 10. From the coordinates given in the figure, we can obtain the hyperradius  $\rho_{3b}$  of such a three-body system, which is given by

$$\rho_{3b}^2 = \frac{m_\alpha a^2}{m} [3 + 4(d/a)^2], \quad (22)$$

where  $m_\alpha$  is the mass of the  $\alpha$  particle and  $m$  is the normalization mass used to define the Jacobi coordinates (the nucleon mass in our calculations).

Also, using the coordinates given in Fig. 10, we can get the moments of inertia relative to each of the three coordinate axes (where axis-3 is perpendicular to the plane containing the three particles shown in the figure). These three moments of

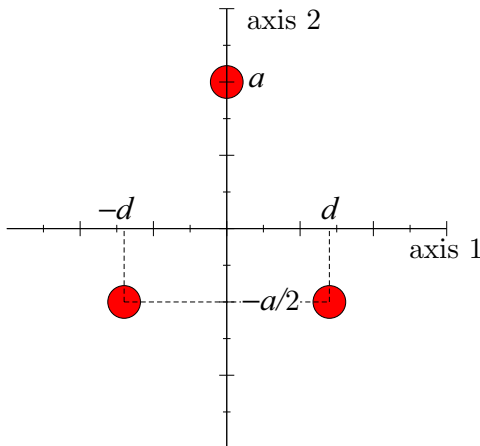


FIG. 10. (Color online) Coordinates of the three-alpha system in the center of mass frame.

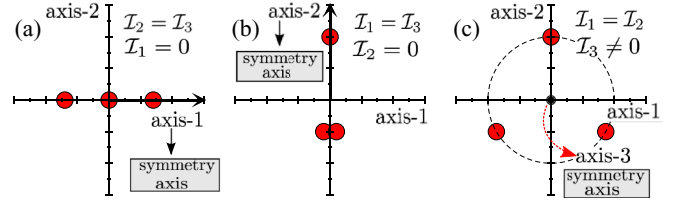


FIG. 11. (Color online) Geometries in the three-alpha system in Fig. 10 corresponding to the symmetry axis along axis-1 (a), along axis-2 (b), and along axis-3 (c). The third axis, axis-3, is perpendicular to the plane holding the three alphas.

inertia take the form

$$\mathcal{I}_1 = \frac{3}{2}m_\alpha a^2, \quad (23)$$

$$\mathcal{I}_2 = 2m_\alpha d^2, \quad (24)$$

$$\mathcal{I}_3 = \mathcal{I}_1 + \mathcal{I}_2 = \frac{3}{2}m_\alpha a^2 + 2m_\alpha d^2, \quad (25)$$

where in  $\mathcal{I}_i$  the index  $i$  refers the axis with respect to which the moment of inertia has been calculated.

We have to keep in mind that in Eqs. (19) and (20) an axial symmetry has been assumed. This implies that these equations can be used in those cases in which two of the moment of inertia in Eqs. (23) to (25) are equal to each other, while the axis with respect to which the moment of inertia is different to the other two defines the symmetry axis [and therefore the  $z$  axis in Eq. (20)]. In other words, there are three possible geometries for the system in Fig. 10 to which Eqs. (19) and (20) can be applied. They are the geometries corresponding to having the symmetry axis along axis-1, axis-2, or axis-3:

(a) *Symmetry axis along axis-1* ( $\mathcal{I}_2 = \mathcal{I}_3$ ). Making equal Eqs. (24) and (25) we get that this happens when  $a = 0$ , leading to  $\mathcal{I}_2 = \mathcal{I}_3 = 2m_\alpha d^2$  and  $\mathcal{I}_1 = 0$ . Making  $a = 0$  corresponds to the geometry shown in Fig. 11(a), where the three alphas are aligned along axis-1, which is the symmetry axis. Therefore, when computing  $Q_0$  by use of Eq. (20) the  $z$  axis has to be taken along axis-1, and for the three-alpha system ( $g_i = 2e$ ) we get  $Q_0 = 8ed^2$ , which by means of Eq. (22) and taking  $m_\alpha/m \approx 4$  can be written as  $Q_0 = e\rho_{3b}^2$ .

(b) *Symmetry axis along axis-2* ( $\mathcal{I}_1 = \mathcal{I}_3$ ). Making now equal Eqs. (23) and (25) we get that this happens when  $d = 0$ , and we get in this case  $\mathcal{I}_1 = \mathcal{I}_3 = 3m_\alpha a^2/2$  and  $\mathcal{I}_2 = 0$ . The corresponding geometry is now the one shown in Fig. 11(b), with the three particles along axis-2, one of them at the position  $a$  and the other two at  $-a/2$ . Taking then axis-2 as the  $z$  axis, we get from Eq. (20) that for the three alphas  $Q_0 = 6ea^2$ , which making use of Eq. (22) can again be written as  $Q_0 = e\rho_{3b}^2$ .

(c) *Symmetry axis along axis-3* ( $\mathcal{I}_1 = \mathcal{I}_2$ ). As before, making equal Eqs. (23) and (24) we find that the symmetry axis is along axis-3 when  $d^2/a^2 = 3/4$ , and  $\mathcal{I}_1 = \mathcal{I}_2 = 3m_\alpha a^2/2$ , and  $\mathcal{I}_3 = 3m_\alpha a^2$ . In this case, the corresponding geometry is the one shown in Fig. 11(c), which corresponds to the three alphas in an equilateral triangle. Taking then the  $z$  axis along axis-3 (perpendicular to the plane holding the three alphas) we get from Eq. (20) that  $Q_0 = -6ea^2$ , or, using again Eq. (22),  $Q_0 = -e\rho_{3b}^2/2$ .

Summarizing, the three axially symmetric geometries shown in Fig. 11 lead to either  $Q_0 = e\rho_{3b}^2$ , which happens

for the linear geometries (a) and (b), or  $Q_0 = -e\rho_{3b}^2/2$ , which happens for the equilateral triangular geometry (c).

As already discussed, our three-body calculations are consistent with  $Q_0 \approx -23 \text{ efm}^2$  for the bound  $2_1^+$  state, as given for instance in Refs. [41,42]. Such a negative value for the intrinsic quadrupole moment is only consistent with  $Q_0 = -e\rho_{3b}^2/2$ , and therefore with the equilateral structure. Furthermore, as shown in Table III, for the states in the first band we have that  $\rho_{\text{rms}} \approx 6.7 \text{ fm}$ , from which we get  $Q_0 = -e\rho_{\text{rms}}^2/2 \approx -22.5 \text{ efm}^2$ . This result is in very good agreement with the computed intrinsic quadrupole moment for the  $2_1^+$  state, the values given in Refs. [41,42], and also with the values given in Table VI for the transitions between the states in the first band. We then conclude that the computed transition strengths and intrinsic quadrupole moments for the transitions between the states in the first band in the three-alpha system are consistent with the ones corresponding to transitions between the states of a rotational band in a three-alpha system where the three alphas are sitting in the vertices of an equilateral triangle.

For the states in the second band, we have from Table III that  $\rho_{\text{rms}} \approx 10 \text{ fm}$ . Using this value we get that for the linear structures in Figs. 11(a) and 11(b) the intrinsic quadrupole moment in the band should be  $Q_0 \approx 100 \text{ efm}^2$ , and for an equilateral triangular arrangement [Fig. 11(c)] it should be  $Q_0 \approx -50 \text{ efm}^2$ . Keeping in mind that, as discussed in connection with Fig. 7(b), the results shown in Table VI for the  $4_1^+ \rightarrow 2_2^+$  transition could have been underestimated, we can conclude that our computed intrinsic quadrupole moments for the states in the second band are consistent with the rotational estimate of  $\sim 100 \text{ efm}^2$  corresponding to the aligned structure shown in either Figs. 11(a) or 11(b).

Another hint about the rotational character of the two bands in  $^{12}\text{C}$  can be given by the sequence of energies in the  $\{0_1^+, 2_1^+, 4_2^+\}$  and the  $\{0_2^+, 2_2^+, 4_1^+\}$  bands. As it is well known, in the case of axial symmetry and  $K = 0$  bands, these energies should follow the rule

$$E_J - E_0 = \frac{\hbar^2}{2\mathcal{I}} J(J+1), \quad (26)$$

where  $E_J$  is the energy of the state in the band with angular momentum  $J$ ,  $E_0$  is the energy of the lowest state in the band, and  $\mathcal{I}$  is the moment of inertia relative to an axis perpendicular to the symmetry axis.

For the three axially symmetric configurations given in Fig. 11 we have

$$\text{Geometry (a): } \mathcal{I} = 2m_\alpha d^2 = m_\alpha \rho_{3b}^2/4, \quad (27)$$

$$\text{Geometry (b): } \mathcal{I} = 3m_\alpha a^2/2 = m_\alpha \rho_{3b}^2/4, \quad (28)$$

$$\text{Geometry (c): } \mathcal{I} = 3m_\alpha a^2/2 = m_\alpha \rho_{3b}^2/8, \quad (29)$$

where, again, we have made use of Eq. (22) with  $a = 0$  in case (a),  $d = 0$  in case (b), and  $d^2/a^2 = 3/4$  in case (c).

For the first band, for which  $E_0 = -7.28 \text{ MeV}$ , the experimental energies of the  $2_1^+$  and  $4_2^+$  states given in Table II lead by means of Eq. (26) to  $\hbar^2/2\mathcal{I} \approx 0.74$  and  $0.71 \text{ MeV}$ , respectively. These values are very similar to each other, supporting the fact that the first band fulfills the condition of a “frozen” structure that gives rise to a rotational band.

Furthermore, this first band has been seen to be consistent with the equilateral triangular structure and  $\rho_{\text{rms}} \approx 6.7 \text{ fm}$ . Making use of Eq. (29) we estimate from the rotational model that  $\hbar^2/2\mathcal{I} \approx 0.9 \text{ MeV}$ , which is relatively close to the values obtained from the experimental  $2_1^+$  and  $4_1^+$  energies.

For the second band, for which  $E_0 = 0.38 \text{ MeV}$ , the energies of the  $2_2^+$  and  $4_1^+$  states in Table II determine  $\hbar^2/2\mathcal{I} \approx 0.33$  and  $0.25 \text{ MeV}$  for the  $2_2^+ \rightarrow 0_2^+$  and  $4_1^+ \rightarrow 2_2^+$  transitions. From the analysis of the intrinsic quadrupole moments we concluded that the states in the second band could at best be consistent with the linear structure in Figs. 11(a) and 11(b), which by use of Eq. (27) or (28), and taking  $\rho_{\text{rms}} \approx 10 \text{ fm}$  (as shown in Table III), lead to the estimate from the rotational model  $\hbar^2/2\mathcal{I} \approx 0.2 \text{ MeV}$ , which is again reasonably consistent with the values obtained from the energy differences. Thus, also in this case the analysis of the energies in the  $\{0_2^+, 2_2^+, 4_1^+\}$  band supports the conclusion obtained from the intrinsic quadrupole moments, namely, the properties of the states in the second band of the three-alpha system are consistent with the behavior expected for states belonging to a rotational band whose structure would be the one in Figs. 11(a) or 11(b).

Although the analysis of both  $Q_0$  and  $\mathcal{I}$  does not permit to distinguish between the linear structures shown in Figs. 11(a) and 11(b), it is important to note that the alpha-alpha Coulomb repulsion clearly prevents the formation of a system as the one described in Fig. 11(b). For this reason, together with the fact that the geometry given in Fig. 11(b) is not consistent with cluster model calculations, we can conclude that the only possible aligned structure for the states in the second band in  $^{12}\text{C}$  is the one given in Fig. 11(a).

We emphasize that our rotational model analysis is schematic, even within our  $\alpha$ -particle model. The  $0^+$  and  $2^+$  bound states are known only to be approximately described by an  $\alpha$ -particle model. The continuum states investigated in this paper are on the other hand expected to be better  $\alpha$ -particle states. However, this does not imply that a schematic classical linear or triangular structure provide an accurate description. Already the quantum mechanical probability distributions differ from this simplified picture. Both an equilateral triangle and a linear chain can only reveal the qualitative essence of the structure of these states. In particular, the accuracy of this illuminating qualitative picture is not in conflict with the bent arm structure of the Hoyle state found in many previous calculations as well as in the present one.

The present interpretation of a rotational band structure is at first glance in conflict with the interpretations of both the  $0_2^+$  and  $2_2^+$  states as a very dilute gas of three particles [43,44]. These two interpretations are difficult to reconcile since a gas of particles does not have rotational states as defined in classical textbooks [30] and used in this paper. Also, the radii of these states in Refs. [43,44] differ apparently from each other, although ascribed to different energies but with “similar structure.” In any case, our conclusions about energies, transition probabilities, and quadrupole moments rely entirely on the computed wave functions. In this sense, interpretations do not play any role since they do not enter into any of the quantum mechanical solutions. Whether these solutions are understood in terms of a frozen intrinsic

structure or a dilute gaslike structure is not important, and both interpretations can in principle be correct simultaneously.

## VII. SUMMARY AND CONCLUSIONS

In this work we investigate the spectrum of  $^{12}\text{C}$  and its rotational character. The existence of two  $0^+$ ,  $2^+$ ,  $4^+$  sequences, related to the  $0_1^+$  ground state and the  $0_2^+$  resonance (the Hoyle state), led people to refer to these two series as rotational bands in  $^{12}\text{C}$ . The sequence,  $0^+$ ,  $2^+$ ,  $4^+$  suggests that the geometry corresponds to axial and  $R_2$  symmetric intrinsic states. However, transitions between rotational states build on different intrinsic shapes with  $K = 0$  band heads would also be mathematically described in precisely the same way. This means that the same tests apply even if other states with different quantum numbers are members of the same band.

In the present case we investigated whether the properties of these continuum states are consistent with the electromagnetic transition strengths for a rotational band built on the ground and first excited  $0^+$  states. In particular, the transition strength should equal the square of the intrinsic quadrupole moment multiplied by a Clebsch-Gordan coefficient.

The three-body wave functions in  $^{12}\text{C}$  have been obtained through the hyperspherical adiabatic expansion method, and the continuum spectrum has been discretized by imposing a box boundary condition on the hyperradius. The discretized continuum spectrum has been obtained on the real energy axis, without preferential treatment of the resonances. Thus, we have from the outset the natural distribution over continuum states. Most existing other models treat resonances as bound states even though many of them have a substantial width. All transition strengths are then present in one wave bound-state-like resonance function.

The transition strength for the different reactions has been extracted from the corresponding  $\gamma$ -emission cross sections. For transitions into a resonance, the calculation of the cross section as a function of the initial three-body energy requires specification of the range of energies investigated in the final state, which should be around the final resonance energy. For this reason, some information about the position of the resonances is needed. In this work this is done by means of the complex scaling method, which provides the resonances as poles of the  $S$  matrix. It is important to emphasize that this is done only to know what energy windows to consider for transitions into a resonance since the method used to discretize the continuum and to compute the cross sections only deals with discretized continuum states with real energies.

From the cross sections two different methods have been used to obtain the transition strengths. The first one uses the  $\Gamma_\gamma$  width as a parameter to fit the peaks of the cross section, associated to resonances in the initial state, with the usual Breit-Wigner shape. From the  $\Gamma_\gamma$  width the transition strength is computed making use of the simple expression relating these two quantities. In the second method, the cross section, as a function of the incident energy, is integrated under the peak corresponding to initial resonance. This integrated cross section gives, except for some known factors, the transition strength.

The cross sections for the  $4^+$  to  $2^+$ , the  $2^+$  to  $0^+$ , and  $2^+$  to  $2^+$  transitions have then been computed. Two different potentials, the Ali-Bodmer and the Buck potentials, have been used to describe the  $\alpha$ - $\alpha$  interaction. The main features of the computed cross sections are in general independent of the potential used. Only those reactions involving resonances whose properties are more sensitive to the potential show a sizable difference in the cross section. This happens for instance in the reactions with initial states with angular momentum and parity  $2^+$ , especially when the lowest  $2^+$  resonance is located at about 1.7 MeV, for which the predicted resonance width differs by a factor of 2 depending on the potential used. In any case, when the energy of the  $2_2^+$  resonance is moved up to 2.4 MeV (in better agreement with the recent experimental value) the dependence on the potential is much less relevant.

The transition strengths obtained from the cross sections are in general consistent with each other. First, the results are similar no matter what method is used to extract the transition strengths ( $\mathcal{B}_\sigma$  or  $\mathcal{B}_\gamma$ ), especially when taking into account the uncertainties inherent to each of the methods. And, second, they are also independent of the potential used. Again, only in the reactions involving the  $2_2^+$  state at 1.7 MeV show a higher dependence on the potential.

The first result we obtained is that the  $4_1^+$  and  $4_2^+$  states, which belong to different bands in  $^{12}\text{C}$  have actually crossed, in such a way that the  $4_1^+$  state belongs to the second band and the  $4_2^+$  to the first one. This is first suggested by the fact that the computed values of  $\rho_{\text{rms}}$ , which should be similar for systems having the same frozen spatial structure, provide values for the  $4_1^+$  state similar to the ones of the  $0_2^+$  and  $2_2^+$  states, and values for the  $4_2^+$  state similar to the ones of the  $0_1^+$  and  $2_1^+$  states. Furthermore, investigating how the  $4_1^+$  and  $4_2^+$  resonances move in the complex energy plane when making the effective three-body force more and more attractive, we have seen that the first  $4^+$  state becoming bound would actually be the  $4_2^+$ .

The assignment of the  $4_1^+$  state to the second band and the  $4_2^+$  to the first is also confirmed by the analysis of the transitions' strengths and the intrinsic quadrupole moments. The values of  $Q_0$  are obtained assuming a rotational character for the two bands in  $^{12}\text{C}$  under investigation, in such a way that the transition strength is basically the square of the intrinsic quadrupole moment multiplied by some geometrical factor depending on the initial and final angular momenta of the transition. Doing like this we have seen that for the  $4_2^+ \rightarrow 2_1^+$  reaction the computed transition strength is clearly more consistent with the previous AMD calculation than the one corresponding to the  $4_1^+ \rightarrow 2_1^+$ . Furthermore, the intrinsic quadrupole moments derived from the transition strengths for the  $2_1^+ \rightarrow 0_1^+$  and  $4_2^+ \rightarrow 2_1^+$  reactions are rather similar and consistent with previous calculations and the experimental value. This consistency would disappear if the reaction  $4_1^+ \rightarrow 2_1^+$  were the one taken into account. The same happens for the reactions in the second band. Although the computed transition strength for the  $4_1^+ \rightarrow 2_2^+$  is even a factor of 3 smaller than the previous AMD calculation, this discrepancy is certainly less important than when considering the  $4_2^+ \rightarrow 2_2^+$  reaction, and it can actually be understood from the uncertainties associated to the method used to extract

the strength. Also, the intrinsic quadrupole moments for the  $2_2^+ \rightarrow 0_2^+$  and  $4_1^+ \rightarrow 2_2^+$  are reasonably stable, stability that would be clearly broken if assuming the  $4_2^+ \rightarrow 2_2^+$  transition as belonging to the second band. Therefore, from the stability of the intrinsic quadrupole moments for each of the  $\{0_1^+, 2_1^+, 4_2^+\}$  and  $\{0_2^+, 2_2^+, 4_1^+\}$  bands we can conclude that each of the bands correspond to states having a rather well-preserved rigid structure.

The rotational character of two bands is confirmed when comparing with the prediction obtained from an axially symmetric rotating structure made by three pointlike alpha particles. Assuming values for  $\rho_{3b}$  similar to the ones computed numerically for the states in the first and second bands ( $\rho_{\text{rms}} \sim 6.7$  fm and  $\sim 10$  fm, respectively) we have seen that the  $Q_0$  values previously computed for the states in the first band are consistent with a equilateral triangular structure rotating around an axis perpendicular to the plane holding the three particles. For the states in the second band, the computed  $Q_0$  values are mostly consistent with a linear distribution of the particles. The same results are obtained from the analyses of the moments of inertia.

Summing up, we have calculated genuine continuum-continuum electric quadrupole ( $E2$ ) transitions from  $0^+$ ,  $2^+$ , and  $4^+$  states in  $^{12}\text{C}$ . The transition strengths are not well defined since neither initial nor final states have well-defined bound-state-like structures in the continuum. Energy windows around resonance positions extending at least the natural widths must contribute to the transitions. Instead, we design, approximate, and deduce correspondingly nonobservable transition strengths from (double) differential cross sections. The results are two sequences of rotational band structures with ground and Hoyle states as band heads with interchange of the order of the two close-lying  $4^+$  resonances. The derived intrinsic quadrupole moments and moments of inertia are consistent with axial triangle and almost linear structures, respectively. In conclusion, our procedure to compute continuum-continuum transitions are used to classify six  $^{12}\text{C}$  states in two rotational bands.

### ACKNOWLEDGMENTS

This work was partly supported by funds provided by DGI of MINECO (Spain) under Contract No. FIS2011-23565. We appreciate valuable continuous discussions with Dr. H. Fynbo and Dr. K. Riisager.

### APPENDIX A: THREE-BODY INCOMING FLUX

Given the three-body reaction  $a + b + c \rightarrow A + \gamma$ , the cross section corresponding to this process requires a definition of the incoming flux of particles. This can be done similarly to the two-body case, where the incoming flux is well defined.

At the two-body level, the Schrödinger equation takes the form

$$i\hbar \frac{\partial \Psi}{\partial t} = -\frac{\hbar^2}{2\mu} \nabla_r^2 \Psi + V\Psi, \quad (\text{A1})$$

where  $\mu$  is the reduced mass,  $\Psi$  the two-body wave function,  $\nabla_r$  is the three-dimensional gradient operator in terms of the relative vector  $\mathbf{r}$ , and  $V$  is the two-body potential. As described in any quantum mechanics textbook, from the Schrödinger equation we can obtain the flux of incoming particles as

$$\mathbf{j} = \frac{1}{2\mu i} [\Psi^* \nabla_r \Psi - (\nabla_r \Psi^*) \Psi], \quad (\text{A2})$$

which for an incoming plane wave leads to the well-known result

$$\mathbf{j} = \hbar \mathbf{p} / \mu, \quad (\text{A3})$$

with  $p$  being the two-body relative momentum.

At the three-body level, the Schrödinger reads as

$$i\hbar \frac{\partial \Psi}{\partial t} = -\frac{\hbar^2}{2\mu_x} \nabla_{r_x}^2 \Psi - \frac{\hbar^2}{2\mu_y} \nabla_{r_y}^2 \Psi + V\Psi, \quad (\text{A4})$$

where now  $\mu_x$  is the reduced mass of two of the particles,  $\nabla_{r_x}$  is the gradient operator in terms of the relative coordinate  $\mathbf{r}_x$  between those two particles,  $\mu_y$  is the reduced mass of the third particle and the two-body system made by the other two, and  $\nabla_{r_y}$  is the gradient operator in terms of the relative coordinate  $\mathbf{r}_y$  between the third particle and the center of mass of the other two. The wave function  $\Psi$  is now a three-body wave function, and  $V$  contains all the potentials involved in the three-body system.

Let us introduce now the usual Jacobi coordinates  $\mathbf{x} = \sqrt{\mu_x/m} \mathbf{r}_x$  and  $\mathbf{y} = \sqrt{\mu_y/m} \mathbf{r}_y$  [22], which contain the arbitrary normalization mass  $m$ . From this definition we immediately get that  $\nabla_{r_x} = \sqrt{\mu_x/m} \nabla_x$  and  $\nabla_{r_y} = \sqrt{\mu_y/m} \nabla_y$ , where  $\nabla_x$  and  $\nabla_y$  are the gradient operators in terms of the  $\mathbf{x}$  and  $\mathbf{y}$  Jacobi coordinates, respectively, and which permit to write the Schrödinger equation (A4) as

$$i\hbar \frac{\partial \Psi}{\partial t} = -\frac{\hbar^2}{2m} \nabla_{x,y}^2 \Psi + V\Psi, \quad (\text{A5})$$

which is equivalent to Eq. (A1) and where we have introduced  $\nabla_{x,y}^2 = \nabla_x^2 + \nabla_y^2$ .

Therefore, from Eq. (A5), and proceeding exactly as done at the two-body level, we can define the three-body incoming flux as

$$\mathbf{j} = \frac{1}{2mi} [\Psi^* \nabla_{x,y} \Psi - (\nabla_{x,y} \Psi^*) \Psi], \quad (\text{A6})$$

where  $\nabla_{x,y}$  is the six-dimensional gradient operator in the Jacobi coordinates  $\mathbf{x}$  and  $\mathbf{y}$ .

Considering now the incoming plane wave  $e^{i(\mathbf{x} \cdot \mathbf{k}_x + \mathbf{y} \cdot \mathbf{k}_y)}$  we get the incoming flux

$$\mathbf{j} = \hbar \frac{(\mathbf{k}_x, \mathbf{k}_y)}{m}, \quad (\text{A7})$$

where  $(\mathbf{k}_x, \mathbf{k}_y)$  represents the six-dimensional momentum given by the three-body momenta  $\mathbf{k}_x$  and  $\mathbf{k}_y$ , which are the momenta associated to the Jacobi coordinates  $\mathbf{x}$  and  $\mathbf{y}$ . If we define now  $\kappa = \sqrt{k_x^2 + k_y^2}$  we then get

$$\mathbf{j} = \hbar \frac{\kappa}{m}, \quad (\text{A8})$$



which is completely analogous to the two-body result in Eq. (A3).

The result given above is correct provided that the wave function  $\Psi$  is normalized to 1 in terms of the Jacobi coordinates  $\mathbf{x}$  and  $\mathbf{y}$ . However, the correct normalization should be done not in terms of the Jacobi coordinates, but in terms of the relative coordinates  $\mathbf{r}_x$  and  $\mathbf{r}_y$ . Since

$$\int d\mathbf{x} d\mathbf{y} |\Psi|^2 = \left(\frac{\mu_x}{m}\right)^{3/2} \left(\frac{\mu_y}{m}\right)^{3/2} \int d\mathbf{r}_x d\mathbf{r}_y |\Psi|^2, \quad (\text{A9})$$

we have that to get  $\Psi$  normalized to 1 in terms of the relative coordinates we have to multiply  $\Psi$  by the factor  $(m/\mu_x)^{3/4}(m/\mu_y)^{3/4}$ , that when done in Eq. (A6) leads to the final expression for the incoming flux:

$$j = \hbar \frac{\kappa}{m} \left(\frac{m}{\mu_x}\right)^{3/2} \left(\frac{m}{\mu_y}\right)^{3/2}. \quad (\text{A10})$$

It is important to note that the flux of particles given above depends on the arbitrary normalization mass  $m$ . This is reflecting the fact that for a given value of the hyperradius  $\rho = \sqrt{x^2 + y^2}$ , the relative distances between the three incoming particles,  $r_x$  and  $r_y$ , will be different for different values of the normalization mass. It is then clear that the flux of particles through some given hypersurface has to depend as well on the choice of  $m$ . The cross section for the reaction  $a + b + c \rightarrow A + \gamma$  is just the flux of outgoing particles normalized with the incoming flux, and therefore, according to Eq. (A10), the cross section will depend as well on  $m$ . In other words, the cross section is only well defined for a given definition of the hyperradius.

### APPENDIX B: CROSS SECTION FOR THE $a + b + c \rightarrow A + \gamma$ PROCESS

As discussed above, the cross section for the process  $a + b + c \rightarrow A + \gamma$  depends on the normalization mass  $m$ . It is not a well-defined physical observable. In fact, the usual observable (therefore independent of  $m$ ) for this kind of reaction is the reaction rate, which after multiplication by the density of particles gives the number of reactions per unit time and unit volume in some specific environment. The reaction rate for the  $a + b + c \rightarrow A + \gamma$  process at a given three-body kinetic energy  $E$ ,  $R_{abc}(E)$ , is given in Eq. (1) of Ref. [45]:

$$R_{abc}(E) = \nu! \frac{\hbar^3}{c^2} \frac{8\pi}{(\mu_x \mu_y)^{3/2}} \frac{2(2J_A + 1)}{(2J_a + 1)(2J_b + 1)(2J_c + 1)} \times \left(\frac{E_\gamma}{E}\right)^2 \sigma_\gamma(E_\gamma), \quad (\text{B1})$$

where  $\nu$  is the number of identical particles in the three-body system,  $J_a$ ,  $J_b$ , and  $J_c$  are the angular momenta of particles  $a$ ,  $b$ , and  $c$ ,  $E_\gamma$  is the photon energy, and  $\sigma_\gamma(E_\gamma)$  is the photodissociation cross section of the process  $A + \gamma \rightarrow a + b + c$ .

The reaction rate is given by the product of the cross section and the incoming flux. Using the expression in Eq. (A10) we can then write

$$R_{abc}(E) = \hbar \frac{\kappa}{m} \left(\frac{m}{\mu_x}\right)^{3/2} \left(\frac{m}{\mu_y}\right)^{3/2} \sigma_{abc}(E), \quad (\text{B2})$$

which after use of Eq. (B1) leads to the following relation between the cross section for the process  $a + b + c \rightarrow A + \gamma$  and the one corresponding to the inverse reaction:

$$\frac{\sigma_{abc}(E)}{\sigma_\gamma(E_\gamma)} = \nu! \frac{2(2J_A + 1)}{(2J_a + 1)(2J_b + 1)(2J_c + 1)} \frac{32\pi}{\kappa^5} \left(\frac{E_\gamma}{\hbar c}\right)^2, \quad (\text{B3})$$

which depends on the normalization mass  $m$  through  $\kappa$ .

### APPENDIX C: REDUCED MATRIX ELEMENT

In this work, the three-body wave functions are written as given in Eq. (9):

$$\Phi_J = \frac{1}{\rho^{5/2}} \sum_n f_n^J(\rho) \phi_n^J(\rho, \Omega). \quad (\text{C1})$$

The angular wave functions  $\phi_n^J(\rho, \Omega)$  in Eq. (C1) are expanded in terms of the hyperspherical harmonics

$$\phi_n^J(\rho, \Omega) = \sum_q C_q^{(n)}(\rho) [\mathcal{Y}_{K\ell_x\ell_y}^L(\Omega) \otimes \chi_{s_x s_y}^S]^J, \quad (\text{C2})$$

where  $q$  collects the quantum numbers  $\{K, \ell_x, \ell_y, L, s_x, S\}$ , where  $K$  is the hypermomentum,  $\ell_x$  and  $s_x$  are the relative angular momentum and total spin of the two particles connected by the  $\mathbf{x}$  Jacobi coordinate,  $\ell_y$  is the relative momentum between the third particle and the center of mass of the first two,  $L$  is the total angular momentum obtained by coupling of  $\ell_x$  and  $\ell_y$ , and  $S$  is the total spin obtained by coupling  $s_x$  and the spin of the third particle  $s_y$ . The total angular momentum  $J$  is obtained by coupling of  $L$  and  $S$ . The total spin function of the three-body system is denoted by  $\chi_{s_x s_y}^S$ , and the hyperspherical harmonics  $\mathcal{Y}_{K\ell_x\ell_y}^L(\Omega)$  are defined as

$$\mathcal{Y}_{K\ell_x\ell_y}^{LM_L}(\Omega) = N_K^{\ell_x\ell_y} (\sin \alpha)^{\ell_x} (\cos \alpha)^{\ell_y} P_\nu^{\ell_x+1/2, \ell_y+1/2}(\cos 2\alpha) \times [Y_{\ell_x}(\Omega_x) \otimes Y_{\ell_y}(\Omega_y)]^{LM_L}, \quad (\text{C3})$$

where  $\nu$  is such that  $K = 2\nu + \ell_x + \ell_y$  and the normalization constant  $N_K^{\ell_x\ell_y}$  can be found for instance in Ref. [22].

For obvious reasons, in order to compute the matrix element  $\langle \Phi_J^{(i)} || y_p^\lambda Y_\lambda(\hat{r}_p) || \Phi_J^{(j)} \rangle$ , it is convenient to write the three-body wave function in terms of the Jacobi set  $\{\mathbf{x}_p, \mathbf{y}_p\}$ . When this is done, insertion of Eqs. (C3) and (C2) into (C1) gives the full expansion of the three-body wave function. Using this expression, the integration over  $\Omega_x$  and  $\Omega_y$  involved in the calculation of the matrix element  $\langle \Phi_{JM}^{(i)} | y_p^\lambda Y_{\lambda\mu}(\hat{r}_p) | \Phi_{J'M'}^{(j)} \rangle$  can be trivially made, and only the integrals over  $\rho$  and  $\alpha$  remain.

After some algebra, we get the final result

$$\begin{aligned} \langle \Phi_J^{(i)} || y_p^\lambda Y_\lambda(\hat{r}_p) || \Phi_{J'}^{(j)} \rangle &= \int d\rho \rho^\lambda \sum_n f_n^J(\rho) \sum_q C_q^{(n)}(\rho) N_K^{\ell_x \ell_y} \sum_{n'} f_{n'}^{J'}(\rho) \sum_{q'} C_{q'}^{(n')}(\rho) N_{K'}^{\ell_x \ell_y} \frac{\hat{\lambda} \hat{\ell}_y \hat{\ell}'_y \hat{L} \hat{L}' \hat{J} \hat{J}'}{\sqrt{4\pi}} \begin{pmatrix} \ell_y & \lambda & \ell'_y \\ 0 & 0 & 0 \end{pmatrix} \\ &\times \begin{Bmatrix} L & \lambda & L' \\ \ell'_y & \ell_x & \ell_y \end{Bmatrix} \begin{Bmatrix} J & J' & \lambda \\ L' & L & S \end{Bmatrix} \frac{(-1)^{J'+\lambda+\ell_x+S}}{2^{a+b+2}} \mathcal{I}_\lambda^{\ell_x \ell_y \ell'_y K K'} \delta_{\ell_x \ell'_x} \delta_{s_x s'_x} \delta_{SS'}, \end{aligned} \quad (C4)$$

where the indices without and with primes refer to the  $\Phi_J^{(i)}$  and  $\Phi_{J'}^{(j)}$  wave functions, respectively,  $\hat{u} = \sqrt{2u+1}$ ,  $a = \ell_x + 1/2$ , and  $b = (\lambda + 1 + \ell_y + \ell'_y)/2$ . Finally,  $\mathcal{I}_\lambda^{\ell_x \ell_y \ell'_y K K'}$  denotes the integral over the hyperangle  $\alpha$ , which can be written as

$$\mathcal{I}_\lambda^{\ell_x \ell_y \ell'_y K K'} = \int_{-1}^1 dx (1-x)^a (1+x)^b P_\nu^{(a, \ell_y+1/2)}(x) P_{\nu'}^{(a, \ell'_y+1/2)}(x). \quad (C5)$$

- 
- [1] F. Hoyle, *Astrophys. J. Suppl. Ser.* **1**, 121 (1954).  
[2] C. W. Cook, W. A. Fowler, C. C. Lauritsen, and T. Lauritsen, *Phys. Rev.* **107**, 508 (1957).  
[3] M. Freer and H. O. U. Fynbo, *Prog. Part. Nucl. Phys.* **78**, 1 (2014).  
[4] F. Ajzenberg-Selove, *Nucl. Phys. A* **506**, 1 (1990).  
[5] M. Freer, H. Fujita, Z. Buthelezi, J. Carter, R. W. Fearick, S. V. Förtsch, R. Neveling, S. M. Pérez, P. Papka, F. D. Smit, J. A. Swartz, and I. Usman, *Phys. Rev. C* **80**, 041303 (2009).  
[6] O. S. Kirsebom *et al.*, *Phys. Rev. C* **81**, 064313 (2010).  
[7] W. R. Zimmerman, M. W. Ahmed, B. Bromberger, S. C. Stave, A. Breskin, V. Dangendorf, Th. Delbar, M. Gai, S. S. Henshaw, J. M. Mueller, C. Sun, K. Tittelmeier, H. R. Weller, and Y. K. Wu, *Phys. Rev. Lett.* **110**, 152502 (2013).  
[8] W. R. Zimmerman, Direct Observation of the Second  $2^+$  State in  $^{12}\text{C}$ , Ph.D. Thesis, University of Connecticut Graduate School 2013, <http://digitalcommons.uconn.edu/cgi/viewcontent.cgi?article=6439&context=dissertations>.  
[9] D. J. Marin-Lambarri, R. Bijker, M. Freer, M. Gai, Tz. Kokalova, D. J. Parker, and C. Wheldon, *Phys. Rev. Lett.* **113**, 012502 (2014).  
[10] R. Álvarez-Rodríguez, E. Garrido, A. S. Jensen, D. V. Fedorov, and H. O. U. Fynbo, *Eur. Phys. J. A* **31**, 303 (2007).  
[11] P. Descouvemont and D. Baye, *Phys. Rev. C* **36**, 54 (1987).  
[12] M. Chernykh, H. Feldmeier, T. Neff, P. von Neumann-Cosel, and A. Richter, *Phys. Rev. Lett.* **98**, 032501 (2007).  
[13] M. Itoh *et al.*, *Nucl. Phys. A* **738**, 268 (2004).  
[14] D. C. Cuong, D. T. Khoa, and Y. Kanada-En'yo, *Phys. Rev. C* **88**, 064317 (2013).  
[15] M. Freer *et al.*, *Phys. Rev. C* **83**, 034314 (2011).  
[16] M. Gai, *J. Phys., Conf. Ser.* **436**, 012007 (2013).  
[17] A. A. Ogloblin, A. S. Demyanova, A. N. Danilov, S. V. Dmitriev, T. L. Belyaeva, S. A. Goncharov, V. A. Maslov, Yu. G. Sobolev, W. Trzaska, and S. V. Khlebnikov, *Eur. Phys. J. Web Conf.* **66**, 02074 (2014).  
[18] R. Bijker and F. Iachello, *Ann. Phys. (NY)* **298**, 334 (2002).  
[19] E. Garrido, A. S. Jensen, and D. V. Fedorov, *Phys. Rev. C* **86**, 064608 (2012).  
[20] E. Garrido, A. S. Jensen, and D. V. Fedorov, *Phys. Rev. C* **88**, 024001 (2013).  
[21] E. Garrido, A. S. Jensen, and D. V. Fedorov, *Few-Body Syst.* **55**, 101 (2014).  
[22] E. Nielsen, D. V. Fedorov, A. S. Jensen, and E. Garrido, *Phys. Rep.* **347**, 373 (2001).  
[23] S. Ali and A. R. Bodmer, *Nucl. Phys. A* **80**, 99 (1966).  
[24] B. Buck, H. Friedrich, and C. Wheatley, *Nucl. Phys. A* **275**, 246 (1977).  
[25] E. Garrido, D. V. Fedorov, and A. S. Jensen, *Nucl. Phys. A* **650**, 247 (1999).  
[26] E. Garrido, D. V. Fedorov, and A. S. Jensen, *Nucl. Phys. A* **617**, 153 (1997).  
[27] C. Forssén, N. B. Shulgina, and M. V. Zhukov, *Phys. Rev. C* **67**, 045801 (2003).  
[28] J. Dohet-Eraly and D. Baye, *Phys. Rev. C* **88**, 024602 (2013).  
[29] J. Dohet-Eraly and D. Baye, *Phys. Rev. C* **90**, 034611 (2014).  
[30] P. J. Siemens and A. S. Jensen, *Elements of Nuclei: Many-body Physics with the Strong Interaction* (Addison-Wesley, New York, 1987), p. 283.  
[31] D. R. Tilley, J. H. Kelley, J. L. Godwin, D. J. Millener, J. Purcell, C. G. Sheu, and H. R. Weller, *Nucl. Phys. A* **745**, 155 (2004).  
[32] Y. K. Ho, *Phys. Rep.* **99**, 1 (1983).  
[33] N. Moiseyev, *Phys. Rep.* **302**, 247 (1998).  
[34] T. Berggren, *Nucl. Phys. A* **109**, 265 (1968).  
[35] T. Berggren, *Phys. Lett. B* **373**, 1 (1996).  
[36] R. Álvarez-Rodríguez, A. S. Jensen, E. Garrido, D. V. Fedorov, and H. O. U. Fynbo, *Phys. Rev. C* **77**, 064305 (2008).  
[37] C. Aa. Diget, Beta delayed particle emission: Probing the triple alpha continuum, Ph.D. Thesis, Natural Science Faculty, University of Aarhus 2006, [http://phys.au.dk/fileadmin/site\\_files/publikationer/phd/Christian\\_Aa\\_Diget.pdf](http://phys.au.dk/fileadmin/site_files/publikationer/phd/Christian_Aa_Diget.pdf).  
[38] A. J. Bartlett, J. A. Tostevin, and I. J. Thompson, *Phys. Rev. C* **78**, 054603 (2008).  
[39] W. Greiner, *Quantum Mechanics: Special Chapters* (Springer, New York, 2001), p. 121.  
[40] A. Bohr and B. R. Mottelson, *Nuclear Structure, Volume II: Nuclear Deformations* (World Scientific, Singapore, 1998), p. 45.  
[41] W. J. Vermeer, M. T. Esat, J. A. Kuehner, R. H. Spear, A. M. Baxter, and S. Hinds, *Phys. Lett. B* **122**, 23 (1983).  
[42] M. Kamimura, *Nucl. Phys. A* **351**, 456 (1981).  
[43] Y. Funaki, A. Tohsaki, H. Horiuchi, P. Schuck, and G. Röpke, *Phys. Rev. C* **67**, 051306 (2003).  
[44] Y. Funaki, A. Tohsaki, H. Horiuchi, P. Schuck, and G. Röpke, *Eur. Phys. J. A* **24**, 321 (2005).  
[45] E. Garrido, R. de Diego, D. V. Fedorov, and A. S. Jensen, *Eur. Phys. J. A* **47**, 102 (2011).